Biological Cybernetics

Analysis of neural clusters due to deep brain stimulation pulses

Daniel Kuelbs[1] · Jacob Dunefsky[2] · Bharat Monga[3] · Jeff Moehlis[4]

Abstract

Deep brain stimulation (DBS) is an established method for treating pathological conditions such as Parkinson's disease, dystonia, Tourette syndrome, and essential tremor. While the precise mechanisms which underly the effectiveness of DBS are not fully understood, several theoretical studies of populations of neural oscillators stimulated by periodic pulses have suggested that this may be related to clustering, in which subpopulations of the neurons are synchronized, but the subpopulations are desynchronized with respect to each other. The details of the clustering behavior depend on the frequency and amplitude of the stimulation in a complicated way. In the present study, we investigate how the number of clusters and their stability properties, bifurcations, and basins of attraction can be understood in terms of one-dimensional maps defined on the circle. Moreover, we generalize this analysis to stimuli that consist of pulses with alternating properties, which provide additional degrees of freedom in the design of DBS stimuli. Our results illustrate how the complicated properties of clustering behavior for periodically forced neural oscillator populations can be understood in terms of a much simpler dynamical system.

Keywords Neural oscillators · Clustering · Phase models · Deep Brain Stimulation

1 Introduction

A primary motivation for this study is Parkinson's disease, which can cause an involuntary shaking that typically affects the distal portion of the upper limbs, and difficulty initiating motion. For patients with advanced Parkinson's disease who do not respond to drug therapy, electrical deep brain stimulation (DBS), an FDA-approved therapeutic procedure,

✉ Jeff Moehlis
  moehlis@ucsb.edu

  Daniel Kuelbs
  dkuelbs@stanford.edu

  Jacob Dunefsky
  jacob.dunefsky@yale.edu

  Bharat Monga
  monga@ucsb.edu

[1] Stanford University, Palo Alto, CA 94305, USA

[2] Yale University, New Haven, CT 06520, USA

[3] Department of Mechanical Engineering, University of California, Santa Barbara, CA 93106, USA

[4] Department of Mechanical Engineering, Program in Dynamical Neuroscience, University of California, Santa Barbara, CA 93106, USA

may offer relief (Benabid et al. 1991). Here, a neurosurgeon guides a small electrode into the sub-thalamic nucleus or globus pallidus interna (GPi); the electrode is connected to a pacemaker implanted in the chest which sends periodic electrical pulses directly into the brain tissue. The efficacy of DBS for the treatment of Parkinson's disease has been found to depend on the frequency of stimulation, with high-frequency stimulation (70 to 1000 Hz and beyond) being therapeutically effective (Benabid et al. 1991; Rizzone et al. 2001; Moro et al. 2002). The generally accepted therapeutic range is 130–180 Hz (Volkmann et al. 2002; Kuncel and Grill 2004). DBS has also shown promising results in treating other neurological conditions, for which the stimulation electrode is implanted in the GPi (for dystonia) or the thalamus (for Tourette syndrome and essential tremor) (Savica et al. 2012; Benabid et al. 2002).

The precise mechanisms which underly the effectiveness of DBS are not fully understood and may be due to inhibition, excitation, disruption, and/or desynchronization of local neural elements; moreover, the mechanism may be different for different stimulation frequencies (Liu et al. 2008; Rosenbaum et al. 2014; Chiken and Nambu 2016; Herrington et al. 2016). In this paper, we draw inspiration from a body of experimental evidence that has suggested that motor symptoms of Parkinson's disease are associated

with pathological synchronization of neurons in the basal ganglia (Uhlhaas and Singer 2006; Chen et al. 2007; Hammond et al. 2007; Levy et al. 2000; Schnitzler and Gross 2005), and theoretical studies that have shown that DBS-like stimulation consisting of periodic pulses applied to neural oscillator populations can lead to chaotic desynchronization (Wilson et al. 2011) or clustering behavior (Wilson and Moehlis 2015), in which subpopulations of the neurons are synchronized, but the subpopulations are desynchronized with respect to each other. Clustering has also been found in theoretical studies of coordinated reset, in which multiple electrodes deliver inputs which are separated by a time delay (Lücken et al. 2013; Lysyansky et al. 2011, 2013; Tass 2003b). These studies, along with clinical successes with coordinated reset (Adamchic et al. 2014), point to clustering as an attractive objective for designing stimulation properties; this has motivated the design of single control inputs which promote clustering (Matchen and Moehlis 2018; Monga and Moehlis 2019; Wilson 2020), in contrast to methods which seek to fully desynchronize the neural activity (Tass 2003a; Nabi et al. 2013; Wilson and Moehlis 2014; Monga and Moehlis 2020). Notably, clustering has at least two important differences from chaotic desynchronization: clustered states often exist over a much larger parameter range than chaotic desynchronization, a possible explanation why effective DBS parameters are easier to find than chaotic desynchronization would suggest; and clustered states may induce plasticity changes more effectively than chaotic desynchronization, which may explain why benefits are more persistent for some kinds of stimulation mechanisms than others (cf. (Adamchic et al. 2014; Monga and Moehlis 2019)). In this paper, we will focus on clustering which arises from a single stimulation electrode, unlike coordinated reset which uses multiple electrodes. It is important to note that clustering is not the normal behavior for neural populations in the basal ganglia. Moreover, note that this framework can also be used to help identify stimuli which lead to desynchronization while *avoiding* clustering, if that is deemed a preferable control objective.

Despite substantial data backing the general efficacy of DBS, it can have side effects including disorientation, memory deficits, spatial delayed recall, response inhibition, episodes of mania, hallucinations, or mood swings, as well as impairment of social functions such as the ability to recognize the emotional tone of a face (Cyron 2016; Buhmann et al. 2017). Our study develops tools which can help to identify different stimuli that result in the same clustering behavior; our hope is that the identification of these alternatives will allow neurologists to consider different stimuli in order to find those which are effective at treating neurological disorders while minimizing the severity of side effects.

In this paper, we investigate how the details of clustering due to periodic pulses of the type used in DBS can be understood in terms of one-dimensional maps defined on the circle.

As a first step, Sect. 2 describes phase reduction, a powerful classical technique for the analysis of oscillators in which a single variable describes the phase of the oscillation with respect to some reference state. Section 3 shows results from simulations of populations of Hodgkin–Huxley neural oscillators stimulated by periodic pulses of the type used for DBS; this illustrates the different types of clustering which can occur and motivates the theoretical analysis. Section 4 derives and investigates the one-dimensional maps which can be used to understand the types of clusters which occur, their stability properties, their bifurcations, and their basins of attraction. Section 5 then demonstrates how this analysis in terms of maps can be generalized to consider stimuli that consist of pulses with alternating properties, which provide additional degrees of freedom for DBS stimulus design. Section 6 summarizes the results. The models for the neurons considered in this paper are given in Appendix A. Simulation and analysis results for thalamic neurons are given in Appendix B; these complement the results on Hodgkin–Huxley neurons from the main text. Appendix C gives theoretical results on how the various maps considered in the paper vary with stimulation parameters.

2 Phase reduction

A common way to describe the dynamics of neurons is to use conductance-based models such as the Hodgkin–Huxley Eqs. (Hodgkin and Huxley 1952). Such models are typically high-dimensional and contain a large number of parameters, which can make them unwieldy for simulations of large neural populations. A powerful technique for the analysis of oscillatory neurons, whose dynamics are described by a stable periodic orbit, is the rigorous reduction in conductance-based models to phase models, with a single variable θ describing the phase of the oscillation with respect to some reference state (Winfree 2001; Kuramoto 1984; Monga et al. 2019).

Suppose that our conductance-based model is described by the n-dimensional dynamical system

$$\frac{d\mathbf{x}}{dt} = \mathbf{F}(\mathbf{x}), \qquad \mathbf{x} \in \mathbb{R}^n \quad (n \geq 2), \tag{1}$$

with a stable periodic orbit $\gamma(t)$ with period T. For each point $\mathbf{x}^*$ in the basin of attraction of $\gamma(t)$, there exists a corresponding phase $\theta(\mathbf{x}^*)$ such that (Guckenheimer 1975; Winfree 2001)

$$\lim_{t \to \infty} \left| \mathbf{x}(t) - \gamma \left(t + \frac{T}{2\pi} \theta(\mathbf{x}^*) \right) \right| = 0, \tag{2}$$

where, under the given vector field, $\mathbf{x}(t)$ is the trajectory of the initial point $\mathbf{x}^*$. The asymptotic phase of $\mathbf{x}$, $\theta(\mathbf{x})$, ranges

in value from $[0, 2\pi)$. In this paper, $\theta = 0$ will represent the phase at which the neuron fires an action potential. Isochrons are level sets of $\theta(\mathbf{x})$, and we define isochrons such that the phase of a trajectory evolves linearly in time both on and off of the periodic orbit (Winfree 1967, 2001). As a result, for the entire basin of attraction of the periodic orbit,

$$\frac{d\theta}{dt} = \frac{2\pi}{T} \equiv \omega. \tag{3}$$

If we now consider the dynamical system

$$\frac{d\mathbf{x}}{dt} = \mathbf{F}(\mathbf{x}) + \mathbf{U}(t), \qquad \mathbf{x} \in \mathbb{R}^n, \tag{4}$$

where $\mathbf{U}(t) \in \mathbb{R}^n$ is an infinitesimal control input, phase reduction gives the one-dimensional system (Kuramoto 1984; Brown et al. 2004; Monga et al. 2019)

$$\frac{d\theta}{dt} = \omega + \mathbf{U}(t)^T \mathbf{Z}(\theta). \tag{5}$$

In this equation, $\mathbf{Z}(\theta)$ is the gradient of θ evaluated on the periodic orbit and is known as the phase response curve (PRC) (Winfree 2001; Ermentrout and Terman 2010; Netoff et al. 2012); it represents the change in phase that the control input will cause when applied at a given phase. In this paper, we consider electrical current inputs which only act in the voltage direction defined by the unit vector $\hat{V}$, i.e., $\mathbf{U}(t) = u(t)\hat{V}$, with the corresponding phase reduction

$$\frac{d\theta_i}{dt} = \omega + Z(\theta_i)u(t). \tag{6}$$

Here, θ_i represents the phase of the ith neuron, ω is the natural frequency of the neuron in radians per second, $Z(\theta) = \frac{\partial\theta}{\partial V}$ is the component of the PRC in the voltage direction, and $u(t)$ is the input. For the populations of neurons considered in this paper, we assume that the neurons are identical and they all receive the same input, and we will consider uncoupled neurons without noise; these assumptions allow a more detailed analysis to be performed.

In the next section, we show simulation results for populations of neurons described by such phase models with periodic pulses of the type used for DBS.

3 Simulation results for identical periodic DBS pulses

In this section, we show simulation results for populations of neurons stimulated by periodic pulses of the type used for DBS; these results will inspire the analysis in Sect. 4. To illustrate a range of clustering behaviors, we show simulations for a prototypical Type II neuron model, the Hodgkin–Huxley
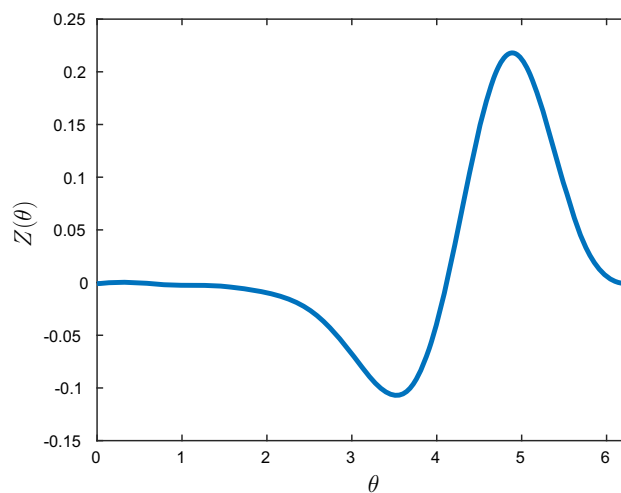

Fig. 1 The phase response curve $Z(\theta)$ for the Hodgkin–Huxley neurons considered in this paper
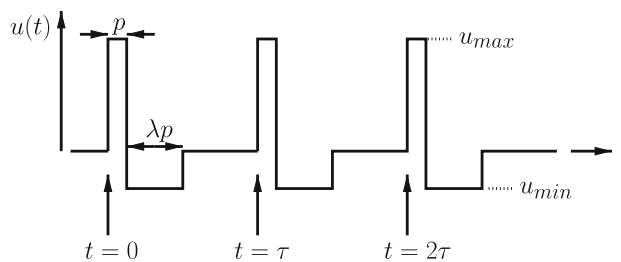

Fig. 2 Periodic sequence of identical pulses

Eqs. (Hodgkin and Huxley 1952). The full equations are given in Appendix A; for our simulations, we use the corresponding phase model. For reference, for these parameters the Hodgkin–Huxley neurons have $\omega = 0.429$ rad/s, and the PRC is shown in Fig. 1. The PRC was calculated numerically using XPP (Ermentrout 2002) and is approximated by a Fourier series. See Appendix B for simulations for an (approximately) Type I neuron model, the thalamic neurons from (Rubin and Terman 2004). These models are not meant to correspond to the neurons directly relevant to Parkinson's disease in human patients; rather, they are used to illustrate typical clustering behaviors for populations of neural oscillators under DBS-like stimuli.

The input $u(t)$ that we consider, shown in Fig.2 and inspired by DBS stimuli (Montgomery 2010), is a τ-periodic sequence of identical charge-balanced pulses parameterized by amplitude u_{max}, period τ (with corresponding frequency $1/\tau$), pulse width p, and multiplier λ (the ratio of time that the pulse is negative to the time that the pulse is positive). Mathematically, $u(t)$ is given by:

$$u(t) = \begin{cases} u_{max} & \text{mod}(t, \tau) \leq p \\ u_{min} \equiv -\frac{u_{max}}{\lambda} & p < \text{mod}(t, \tau) \leq (\lambda + 1)p \\ 0 & \text{otherwise.} \end{cases} \tag{7}$$

Unless otherwise stated, we will use u_{max} corresponding to a current density of $20\mu A/cm^2$, $p = 0.5$ ms, and $\lambda = 3$ in our simulations. We consider different frequencies of stimulation between 70–300 Hz, which includes the typical therapeutic range of 130–180 Hz for DBS treatment of Parkinson's disease.

We simulated 500 Hodgkin–Huxley neurons with initial phases evenly spaced between 0 and 2π, corresponding to an initial uniform phase distribution. The stimulation frequency was varied from 70 Hz to 300 Hz in increments of 5 Hz. Figure 3a shows the final phases after 40 periods of stimulation, after transients have decayed away. The colors indicate the initial phases of the neurons. Not all colors are visible for most stimulation frequencies because the final phases of entire subpopulations of neurons are nearly identical, and only one representative initial phase can be seen. All of the neurons which have nearly the same final phase are part of the same cluster. Figure 3b shows the generalized order parameters (Daido 1996)

$$r_m = \frac{1}{N} \left| \sum_{j=1}^{N} e^{im\theta_j} \right|, \qquad (8)$$

for $m = 1, 2, 3$. These help to identify cluster states. For example, when the neurons all have the same phase (corresponding to a single cluster), $r_1 = r_2 = r_3 = 1$. When there are two equally populated clusters with a phase difference of π, $r_1 = r_3 = 0$ and $r_2 = 1$. When r_3 is large and r_1 and r_2 are small, we expect that the system is in a state with three clusters. A uniform phase distribution will have $r_1 = r_2 = r_3 = 0$.

Figure 4 shows the times series of the phases of a population of Hodgkin–Huxley neurons for selected frequencies and helps us to interpret the results shown in Fig. 3. For example, Fig. 4a shows that for a 100 Hz stimulus the neurons separate into three clusters, as is also the case for 250 Hz as shown in Fig. 4e. (Notice that Fig. 3 shows three possible final phases and high values for r_3 for each of these frequencies, corresponding to these three clusters.) Fig. 4b shows that for a 150 Hz stimulus the neurons separate into two clusters. For a 180 Hz stimulus, there is no clustering; see Fig. 4c; we will argue below that this corresponds to chaotic dynamics. By carefully looking at Fig. 4d, one sees that for a 185 Hz stimulus there are five clusters, as expected from final states shown at this frequency in Fig. 3. Such clustering behavior and non-clustering (chaotic) behavior have been seen in other studies, such as (Wilson et al. 2011) and (Wilson and Moehlis 2015).

Inspired by neural synchrony in Parkison's patients, we also considered an initial partially synchronized neural population, with phases distributed according to a von Mises
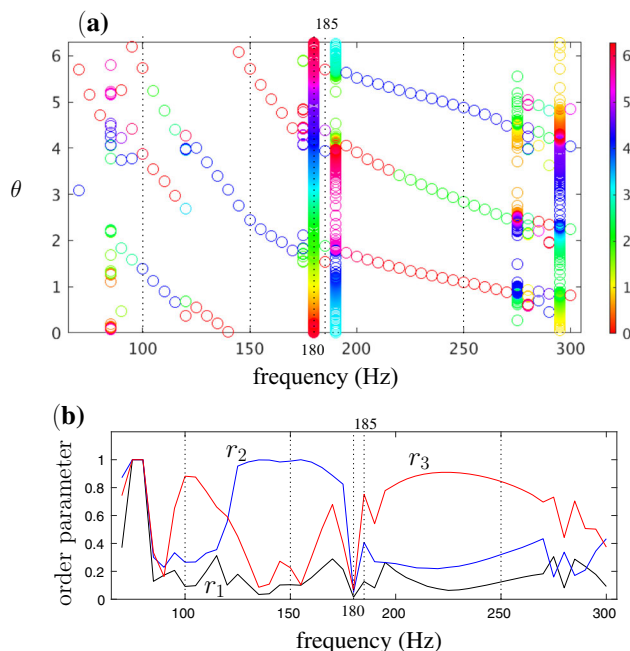

Fig. 3 **a** The final phases θ of Hodgkin–Huxley neurons drawn from an initial uniform distribution as a function of stimulation frequency, after 40 periods of stimulation. Colors correspond to the neurons' initial phases. Not all colors are visible for most stimulation frequencies because the final phases of entire subpopulations of neurons are nearly identical, and only one representative initial phase can be seen. The vertical dotted lines correspond to frequencies shown in Fig. 4. **b** Order parameters r_1 (black), r_2 (blue), and r_3 (red) for the final state as a function of frequency. For the initial uniform distribution, $r_1 = r_2 = r_3 = 0$

distribution (Best and Fisher 1979) centered at $\theta = 0$:

$$\rho_0(\theta) = \frac{e^{\kappa \cos\theta}}{2\pi I_0(\kappa)}, \qquad (9)$$

where $I_0(\kappa)$ is the modified Bessel function of order 0. This distribution is similar to a Gaussian distribution, but on a circle. We simulated 500 Hodgkin–Huxley neurons with initial phases distributed according to the von Mises distribution with $\kappa = 50$. As for Fig. 3, the stimulation frequency was varied from 70 Hz to 300 Hz in increments of 5 Hz. Fig. 5a shows the final phases after 40 periods of stimulation, after transients have decayed away. We see that the final phases of the neurons from the initial von Mises distribution lie on a subset of the final phases of the neurons from the initial uniform distribution. For example, when the stimulation frequency is 100 Hz, the neurons from the initial von Mises distribution are concentrated in two of the three clusters which exist for the initial uniform distribution. From Fig. 5b, the initial state is highly synchronized, and there are limited frequencies for which these deviate significantly from their initial values. Note that often a single cluster forms, which has $r_1 = r_2 = r_3 = 1$.
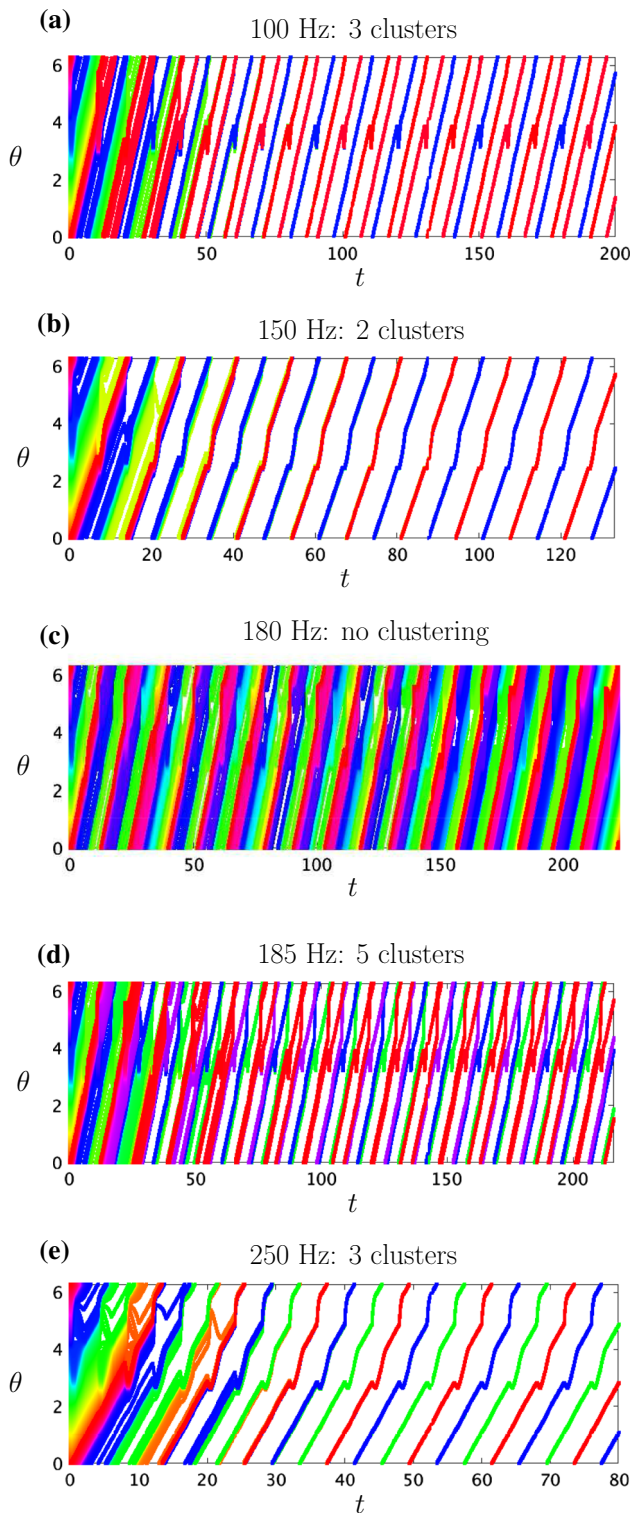
(a)

(b)

(c)

(d)

(e)

Fig. 4 Time series showing the phases of Hodgkin–Huxley neurons drawn from an initial uniform distribution for frequencies **a** 100 Hz, **b** 150 Hz, **c** 180 Hz, **d** 185 Hz, and **e** 250 Hz. The titles of these panels indicate the number of clusters found after transients have decayed away. For (c), clusters do not form. For this and subsequent time series figures, t is measured in ms, and the colors indicate the initial phases of the neurons, with colorbar as in Fig. 3
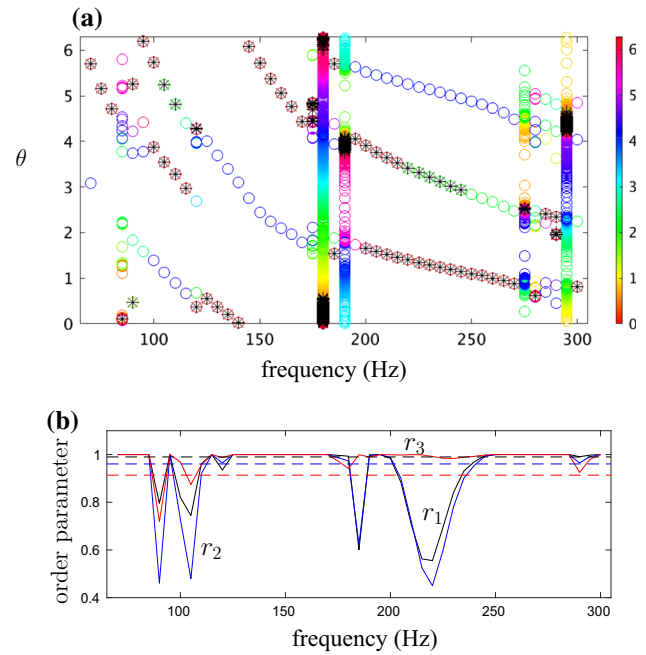
(a)

(b)

Fig. 5 **a** As a function of stimulation frequency, the final phases θ of Hodgkin–Huxley neurons drawn from an initial von Mises distribution after 40 periods of stimulation are shown as black ∗'s, overlaid on the final phases of Hodgkin–Huxley neurons drawn from an initial uniform distribution (as was shown in Fig. 3). **b** Order parameters r_1 (black), r_2 (blue), and r_3 (red) as a function of frequency, with their initial values shown as dashed lines

We also designed an algorithm to detect the size of clusters in a population. The algorithm groups the phases of neurons in a population at each timestep into clusters by sorting the phases in ascending order and checking if the ith phase is within ϵ of the $(i + 1)$-th phase for an appropriate small value of ϵ. If so, the size of the current cluster is increased by one. If not, the algorithm creates a new cluster. The process is repeated until all neurons have been grouped into clusters. Figure 6 shows the number of neurons in the different clusters over a range of frequencies for the initial uniform distribution (for which three clusters are populated) and von Mises distribution (for which only two clusters are populated). As we will see in Sect. 4, this figure can be explained in terms of the basins of attraction of fixed points of iterates of a one-dimensional map defined on the circle. The initial phase of a given neuron will determine which cluster it ends up in. These maps will also allow us to understand the types of clusters which occur in these simulations, along with their stability properties, and bifurcations. Note that Appendix B shows simulation results for populations of thalamic neurons with the same stimuli (7).
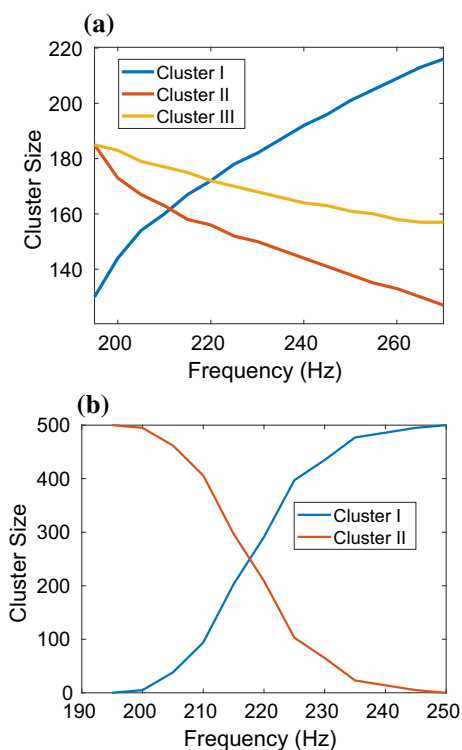
Fig. 6 The number of Hodgkin–Huxley neurons in different clusters for a population size of 500, with initial **a** uniform and **b** von Mises distributions

4 Analysis of clusters due to identical pulses using 1D maps

In this section, we show how the clustering behavior found in the simulations from Sect. 3 can be understood in terms of appropriate compositions of one-dimensional maps on the circle. We note that the use of one-dimensional maps to describe the dynamics of neural and other biological systems has a rich history, e.g., (Keener et al. 1981; Glass and Mackey 1988; Ermentrout and Kopell 1998; Ermentrout and Terman 2010).

We consider a system of neural oscillators subjected to a τ-periodic sequence of pulses as shown in Fig. 2 and described by the dynamics (Wilson and Moehlis 2015)

$$\dot{\theta}_i = \omega + f(\theta_i)\delta(\mathrm{mod}(t, \tau)), \qquad i = 1, \cdots, N. \tag{10}$$

Here, the response function $f(\theta)$ describes the change in phase due to a single pulse (including the positive current for time p, and the negative current for time λp). If the pulse was a delta function with unit area, $f(\theta)$ would be equal to the infinitesimal PRC $Z(\theta)$; for more general pulses, it can be calculated using a direct method in which a pulse is applied at a known phase, and the change in phase is deduced from the change in timing of the next action potential (Netoff et al. 2012). We will think of the change in phase due to the
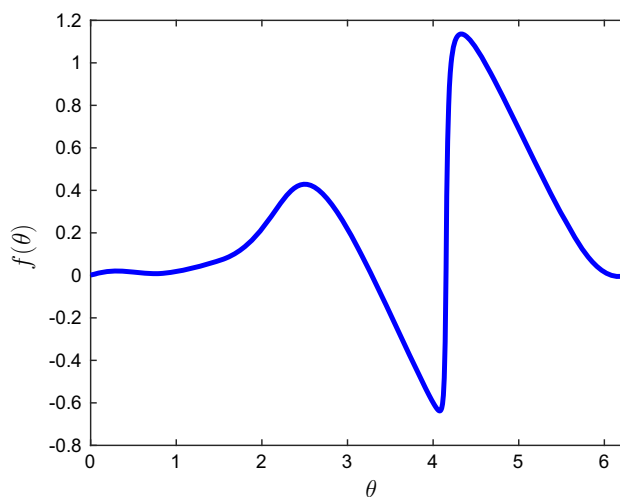

Fig. 7 Response function $f(\theta)$ which characterizes the phase response of Hodgkin–Huxley neurons to the stimulus, for u_{max} corresponding to a current density of $20\mu A/cm^2$, $p = 0.5$ ms, and $\lambda = 3$

pulse as occurring instantaneously, even though the pulse will typically have a finite duration; this will be a good approximation for pulses of short duration. Figure 7 shows $f(\theta)$ for the Hodgkin–Huxley neurons considered in this paper for pulses as shown in Fig. 2 with u_{max} corresponding to a current density of $20\mu A/cm^2$, $p = 0.5$ ms, and $\lambda = 3$.

To understand the clustering behavior, it will be useful to consider the map which takes the phase of a neuron to the phase exactly one forcing cycle later, cf. (Wilson and Moehlis 2015). To find this map, suppose that we start with $\theta(0^+) = \theta_0$, immediately after the start of a pulse, where we assume that we have already accounted for the effect of the pulse according to the function $f(\theta)$. The next pulse comes at time τ. Up until time τ, the phase evolves according to $\dot{\theta} = \omega$; therefore,

$$\theta(\tau^-) = \theta_0 + \omega\tau. \tag{11}$$

Treating the change in phase due to the next pulse as occurring instantaneously, we have

$$\theta(\tau^+) = \theta_0 + \omega\tau + f(\theta_0 + \omega\tau). \tag{12}$$

The system then evolves for a time τ without stimulus, giving

$$\theta(2\tau^-) = \theta_0 + 2\omega\tau + f(\theta_0 + \omega\tau); \tag{13}$$

the next pulse at time 2τ gives

$$\begin{aligned}\theta(2\tau^+) = {} & \theta_0 + 2\omega\tau + f(\theta_0 + \omega\tau) \\ & + f(\theta + 2\omega\tau + f(\theta_0 + \omega\tau)),\end{aligned} \tag{14}$$

and so on. It is useful to let (Wilson and Moehlis 2015)

$$g(s) = s + \omega\tau + f(s + \omega\tau), \tag{15}$$

which gives

$$\theta(n\tau^+) = g^{(n)}(\theta_0), \tag{16}$$

where $g^{(n)}$ denotes the composition of g with itself n times, and θ_0 is the initial state of the neuron.

We look for fixed points of $g^{(n)}$, that is, solutions to $\theta^* = g^{(n)}(\theta^*)$; for such solutions, the phase has the same value after n pulses as where it started. We are particularly interested in fixed points of $g^{(n)}$ which are not fixed points of $g^{(m)}$ for any positive integer m satisfying $m < n$; then, there will be n fixed points of $g^{(n)}$ that correspond to points on a period-n orbit of g. If

$$\left| \frac{d}{d\theta} \right|_{\theta=\theta^*} (g^{(n)}(\theta)) \right| < 1, \tag{17}$$

then the fixed point θ^* of $g^{(n)}$ is stable, as is the corresponding period-n orbit of g. Neurons which start with initial phases within the basin of attraction of a given fixed point of $g^{(n)}$ will asymptotically approach that fixed point under iterations of $g^{(n)}$. The n different fixed points will each have a basin of attraction, so a uniform initial distribution of neurons will form n clusters, one for each of these fixed points of $g^{(n)}$, cf. (Wilson and Moehlis 2015).

We note some useful properties of g and its iterates. First, consider $g_\tau(\theta)$ corresponding to a τ-periodic sequence of pulses (that is, with frequency $1/\tau$), and $g_\sigma(\theta)$ corresponding to a σ-periodic sequence of pulses (that is, with frequency $1/\sigma$). Letting

$$\theta = \hat{\theta} + \omega(\tau - \sigma), \tag{18}$$

we see that

$$\begin{aligned} g_\sigma(\theta) &= \hat{\theta} + \omega(\tau - \sigma) + \omega\sigma + f(\hat{\theta} + \omega(\tau - \sigma) + \omega\sigma) \\ &= \hat{\theta} + \omega\tau + f(\hat{\theta} + \omega\tau) = g_\tau(\hat{\theta}). \end{aligned}$$

Therefore,

$$g_\sigma(\theta) = g_\tau(\theta + \omega(\sigma - \tau)). \tag{19}$$

For $\sigma < \tau$, σ-periodic forcing has a higher frequency $(1/\sigma)$ than τ-periodic forcing (frequency $1/\tau$); thus, we see that the function g keeps the same shape and shifts to the right as the forcing frequency increases; see the top panel of Fig. 8.

Although this shift property is not true for higher iterates of g, it does hold approximately, as shown in Proposition 1 of Appendix C and illustrated in the bottom panel of Fig. 8:

$$g_\sigma^{(n)}(\theta) = g_\tau^{(n)}(\theta + \omega(\sigma - \tau)) + \mathcal{O}(\sigma - \tau). \tag{20}$$

We now illustrate how these maps can be used to understand the specific clustering behavior shown in Sect. 3. Figure 8 shows $g(\theta)$ and $g^{(2)}(\theta)$ for various frequencies. We see, for example, that there are two fixed points for g for 80 Hz, one stable (the slope at the intersection is between -1 and $+1$) and one unstable (the slope at the intersection is greater than 1), corresponding to a stable and an unstable single cluster, respectively. In such a cluster, all neurons have identical phases, giving synchrony. This explains the single value of the final phase for 80 Hz in Fig. 3. As the frequency increases (and g shifts to the right), these fixed points annihilate in a saddlenode bifurcation (which occurs at the frequency at which g becomes tangent to the diagonal), so that at 90 Hz there are no fixed points of g.

From Fig. 8, we can also deduce the presence of saddle-node bifurcations for the $g^{(2)}$ map as it shifts right with small corrections according to (20) as the frequency increases, leading to 2-cluster states for a range of frequencies. For example, suppose that a population of Hodgkin–Huxley neurons is stimulated with frequency 150 Hz, corresponding to $\tau = 6.67$ ms. We see that there are two stable fixed points for $g^{(2)}(\theta)$, at $\theta = 2.86$ and $\theta = 5.86$ (these fixed points are stable because the slope at the intersection is between -1 and $+1$). There are also two unstable fixed points for $g^{(2)}$ at $\theta = 1.305$ and $\theta = 4.685$, where the slope at the intersection is greater than 1. There are no fixed points for $g(\theta)$ for 150 Hz, but a cobweb analysis verifies that there is a period-2 orbit

$$\theta = 2.86 \rightarrow 5.86 \rightarrow 2.86 \rightarrow \cdots.$$

These fixed points of $g^{(2)}$ correspond a stable 2-cluster state for a population of oscillators, as shown in Fig. 4b. We note that we can deduce the basin of attraction for the different stable fixed points of $g^{(2)}$; for example, the basin of attraction for the stable fixed point at $\theta = 2.86$ is the range $1.305 < \theta_0 < 4.685$, that is, between the two unstable fixed points. This analysis of the $g^{(2)}$ maps explains the two values of the final phase for the range from approximately 125 Hz to 170 Hz in Fig. 3.

As another example, suppose that a population of Hodgkin–Huxley neurons is stimulated with frequency 100 Hz, corresponding to $\tau = 10$ ms. Figure 9 shows $g(\theta)$ and $g^{(3)}(\theta)$, the latter for a range of frequencies. We see that for 100 Hz, there are three stable fixed points for $g^{(3)}(\theta)$, at $\theta = 1.43$, $\theta = 3.37$, and $\theta = 5.86$ (these fixed points are stable because the slope at the intersection has slope between -1 and $+1$). There are no fixed points for $g(\theta)$, but a cobweb
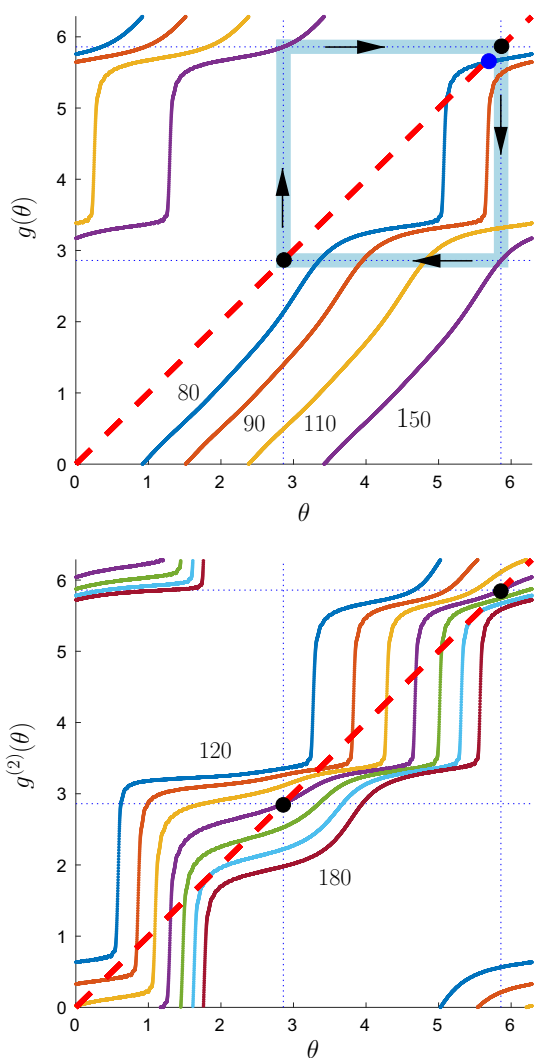
Fig. 8 Maps $g(\theta)$ with stimulation frequencies 80, 90, 110, and 150 Hz, and $g^{(2)}(\theta)$ with stimulation frequencies 120, 130, 140, 150, 160, 170, and 180 Hz for Hodgkin–Huxley neurons. Intersections with the diagonal dashed line indicate fixed points of the respective map. The dotted lines show θ values for the stable fixed points of the $g^{(2)}$ map for 150 Hz, corresponding to the period-2 orbit for g
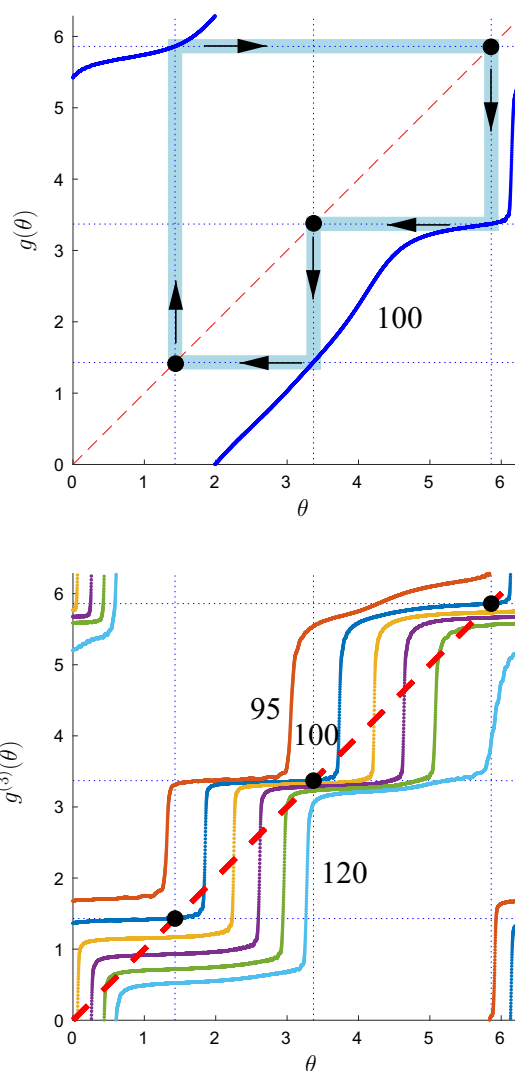
Fig. 9 Maps $g(\theta)$ for stimulation frequency 100 Hz, and $g^{(3)}(\theta)$ for Hodgkin–Huxley neuron for stimulation frequencies 95, 100, 105, 110, 115, and 120 Hz

analysis verifies that there is a period-3 orbit

$$\theta = 1.43 \rightarrow 5.86 \rightarrow 3.37 \rightarrow 1.43 \rightarrow \cdots .$$

These fixed points of $g^{(3)}$ correspond a stable 3-cluster state for a population of oscillators, as shown in Fig. 4a. We can deduce the presence of saddlenode bifurcations for the $g^{(3)}$ map as it shifts right (with small corrections) as the frequency increases, leading to 3-cluster states. This explains the three values of the final phase for the range from approximately 100 Hz to 115 Hz in Fig. 3.

We can understand the cluster sizes shown in Fig. 6a by looking at the basins of attraction of the different stable fixed points, as indicated in Fig. 10 for 200 Hz and 260 Hz stim-

uli. The basin boundaries are at the phases of the appropriate unstable fixed points. When the initial phase distribution is uniform, the number of neurons which end up in each cluster is proportional to the size of the corresponding basin of attraction. For example, if there are 500 uniformly distributed neurons, this predicts that there will be 144, 173, and 183 neurons in Clusters I, II, and III, respectively, for a 200 Hz stimulus, and 209, 133, and 159 neurons in Clusters I, II, and III, respectively, for a 260 Hz stimulus. This is consistent with the results shown in Fig. 6a. The number of neurons in each cluster for Fig. 6b would be determined by the number of neurons which are initially in the respective basin of attraction, as determined by the initial phase distribution; here, there were no neurons with initial phases that end up in Cluster III.
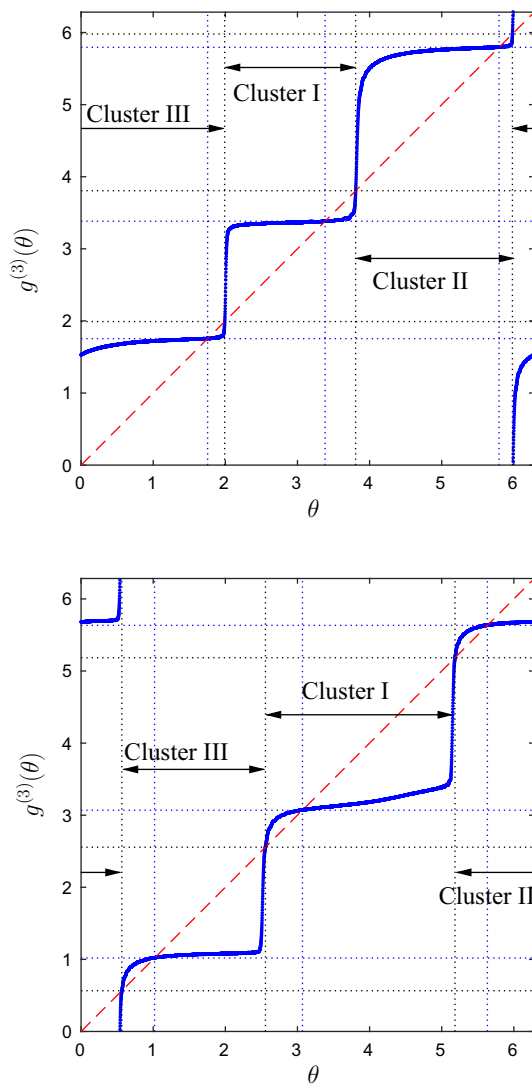
Fig. 10 Basins of attraction for the different clusters for **a** 200 Hz and **b** 260 Hz stimuli

Finally, we can use g to calculate the Lyapunov exponent Λ associated with the attractors for the map g. This is of interest because it identifies stimulation frequencies which give chaotic dynamics ($\Lambda > 0$) or non-chaotic states including stable clusters and the fully synchronized state ($\Lambda < 0$). Specifically (Ott 1993),

$$\Lambda = \lim_{n \to \infty} \frac{1}{n} \sum_{j=0}^{n-1} \log g'(\theta_j), \tag{21}$$

where θ_0 is a point on the attractor. Here, $g'(\theta) = 1 + f'(\theta + \omega\tau)$. We chose an initial phase and iterated the map for 1000 iterates to get rid of transients and then averaged the next 49000 iterates. Results are shown in Fig. 11. For example, for stimulation frequency 180 Hz, we find $\Lambda = 0.29$, which is consistent with the non-clustering dynamics shown in Fig. 4c;
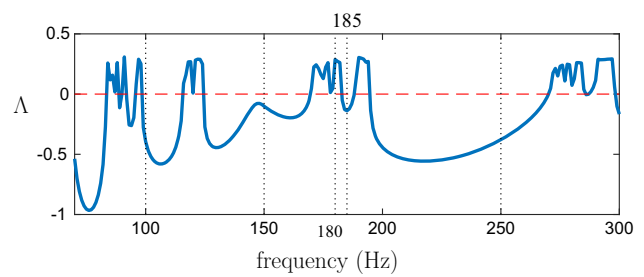

Fig. 11 Lyapunov exponent Λ as a function of stimulation frequency for Hodgkin–Huxley neurons. The vertical dotted lines correspond with the frequencies shown in Fig. 4
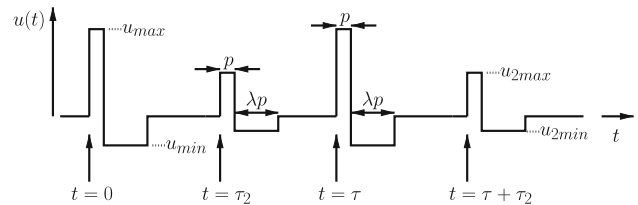

Fig. 12 Sequence of alternating pulses

for stimulation frequency 150 Hz, which gives a stable 2-cluster state, $\Lambda = -0.098$.

5 Analysis of clusters due to pulses with alternating properties using 1D maps

In this section, we consider more general stimuli, specifically pulses with alternating properties, as shown in Fig. 12. These provide additional degrees of freedom in the design of DBS stimuli. Here, the pulses from before, that is with u_{max} corresponding to a current density of $20\mu A/cm^2$, $p = 0.5$ ms, and $\lambda = 3$, will be assumed to occur at times $0, \tau, 2\tau, \cdots$. But now additional pulses with u_{2max} corresponding to a current density of $10\mu A/cm^2$, $\lambda = 3$, $u_{2min} = -u_{2max}/\lambda$ and $p = 0.5$ ms, will be assumed to occur at times $\tau_2, \tau + \tau_2, 2\tau + \tau_2, \cdots$. Figure 13 shows that the clustering behavior for such alternating pulses with $\tau_2 = \tau/2$ strongly resembles the clustering behavior found at twice the frequency for identical pulses, as shown in Fig. 3, although there are differences. The analysis in this section shows how the methods from Sect. 4 can be adapted to understand clustering behavior for such alternating pulses.

It will again be useful to consider the map which takes the phase of a neuron to its phase at a time τ later. To formulate this map, we need the response curves for each type of pulse: the response curve $f(\theta)$ for the pulse with u_{max} corresponding to $20\mu A/cm^2$ was already shown in Fig. 7; the response curve $f_2(\theta)$ for the pulse with u_{max} corresponding to $10\mu A/cm^2$ is shown in Fig. 14. To find this map, suppose that we start with $\theta(0^+) = \theta_0$, immediately after the start of
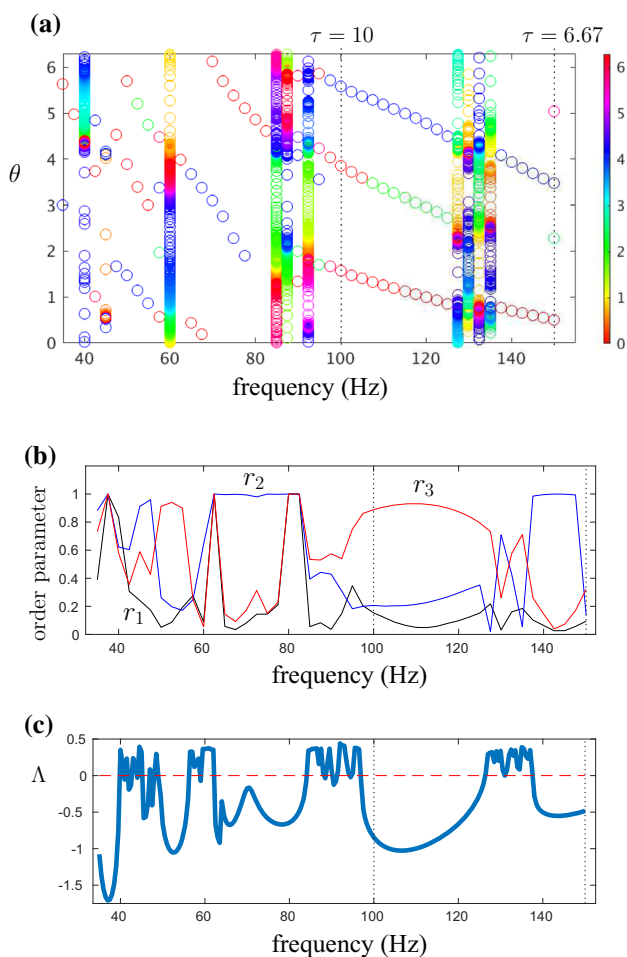
(a)

(b)

(c)

Fig. 13 **a** The final phases θ of Hodgkin–Huxley neurons drawn from an initial uniform distribution as a function of stimulation frequency, after 80 periods of pulses with alternating properties (to allow transients to decay), as described in the text. Colors correspond to the neurons' initial phases. The vertical dotted lines correspond to stimulation frequencies which are analyzed in more detail in the main text. **b** Order parameters r_1 (black), r_2 (blue), and r_3 (red) for the final state as a function of frequency. For the initial uniform distribution, $r_1 = r_2 = r_3 = 0$. **c** Lyapunov exponent Λ as a function of stimulation frequency

a pulse, where we assume that we have already accounted for the effect of the pulse according to the function $f(\theta)$. The next pulse, of different type, comes at time τ_2. Up until time τ_2, the phase evolves according to $\dot{\theta} = \omega$; therefore,

$$\theta(\tau_2^-) = \theta_0 + \omega\tau_2. \tag{22}$$

Treating the change in phase due to the next pulse as occurring instantaneously, we have

$$\theta(\tau_2^+) = \theta_0 + \omega\tau_2 + f_2(\theta_0 + \omega\tau_2). \tag{23}$$
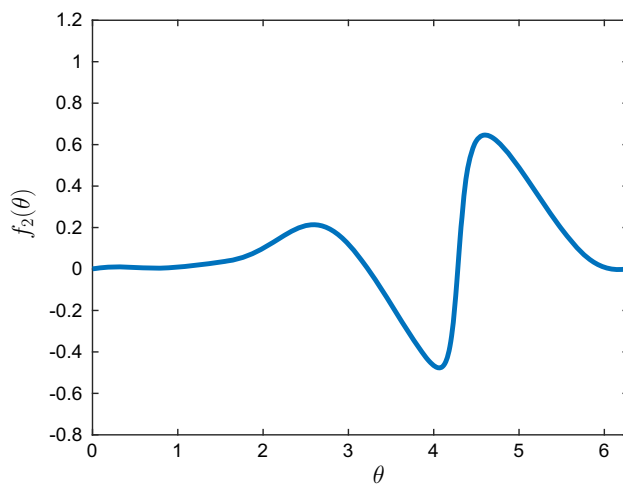
Fig. 14 Response function $f_2(\theta)$ which characterizes the phase response of a Hodgkin–Huxley neuron to a pulse with u_{2max} corresponding to a current density of $10\mu A/cm^2$, $u_{2min} = -u_{2max}/3$, and $p = 0.5$ ms

The system then evolves for a time $\tau - \tau_2$ without stimulus, giving

$$\theta(\tau^-) = \theta_0 + \omega\tau_2 + \omega(\tau - \tau_2) + f_2(\theta_0 + \omega\tau_2)$$
$$= \theta_0 + \omega\tau + f_2(\theta_0 + \omega\tau_2).$$

At time τ, we have another pulse of the type that started at $t = 0$, so

$$\theta(\tau^+) = \theta_0 + \omega\tau + f_2(\theta_0 + \omega\tau_2)$$
$$+ f(\theta_0 + \omega\tau + f_2(\theta_0 + \omega\tau_2)).$$

Continuing in this fashion, we obtain

$$\theta(\tau + \tau_2^-) = \theta_0 + \omega(\tau + \tau_2) + f_2(\theta_0 + \omega\tau_2)$$
$$+ f(\theta_0 + \omega\tau + f_2(\theta_0 + \omega\tau_2)),$$
$$\theta(\tau + \tau_2^+) = \theta_0 + \omega(\tau + \tau_2) + f_2(\theta_0 + \omega\tau_2)$$
$$+ f(\theta_0 + \omega\tau + f_2(\theta_0 + \omega\tau_2))$$
$$+ f_2(\theta_0 + \omega(\tau + \tau_2) + f_2(\theta_0 + \omega\tau_2)$$
$$+ f(\theta_0 + \omega\tau + f_2(\theta_0 + \omega\tau_2)))$$
$$\theta(2\tau^-) = \theta_0 + 2\omega\tau + f_2(\theta_0 + \omega\tau_2)$$
$$+ f(\theta_0 + \omega\tau + f_2(\theta_0 + \omega\tau_2))$$
$$+ f_2(\theta_0 + \omega(\tau + \tau_2) + f_2(\theta_0 + \omega\tau_2)$$
$$+ f(\theta_0 + \omega\tau + f_2(\theta_0 + \omega\tau_2)))$$
$$\theta(2\tau^+) = \theta(2\tau^-) + f(\theta(2\tau^-)).$$

A useful formulation is to let

$$G(s) = s + \omega\tau + f_2(s + \omega\tau_2) + f(s + \omega\tau$$
$$+ f_2(s + \omega\tau_2)), \tag{24}$$

which gives

$$\theta(n\tau^+) = G^{(n)}(\theta_0). \tag{25}$$

Proposition 2 in Appendix C shows that G and its iterates have an approximate shift property when τ and/or τ_2 are changed to nearby values, which will be useful for understanding bifurcations of the cluster states. In particular, letting $G_{\tau,\tau_2}(\theta)$ be the map for G corresponding a sequence of alternating pulses with parameters τ and τ_2,

$$G_{\sigma,\sigma_2}^{(n)} = G_{\tau,\tau_2}^{(n)}(\theta + \omega(\sigma - \tau) + \omega(\sigma_2 - \tau_2))$$
$$+ \mathcal{O}(\sigma - \tau) + \mathcal{O}(\sigma_2 - \tau_2) \tag{26}$$

for $n \geq 1$. Note that there are $\mathcal{O}(\sigma - \tau)$ and $\mathcal{O}(\sigma_2 - \tau_2)$ corrections even for $n = 1$.

Alternatively, we can view G as a composition of two maps:

$$\theta(0^+) = \theta_0,$$
$$\theta(\tau_2^+) = \theta_0 + \omega\tau_2 + f_2(\theta_0 + \omega\tau_2) \equiv h_2(\theta_0),$$
$$\theta(\tau^+) = \theta(\tau_2^+) + \omega(\tau - \tau_2) + f(\theta(\tau_2^+) + \omega(\tau - \tau_2))$$
$$\equiv h_1(\theta(\tau_2^+)) = h_1(h_2(\theta_0)) = G(\theta_0).$$

Note that we have written G, which is a map over the time interval τ, as the composition of two maps h_1 and h_2, that is,

$$G = h_1 \circ h_2.$$

These maps h_1 and h_2 also have shift properties. In particular, letting $h_{1\tau,\tau_2}(\theta)$ be the h_1 map for a sequence of alternating pulses with parameters τ and τ_2, and letting $h_{2\tau_2}$ be the h_2 map for a sequence of alternating pulses with parameter τ_2, Proposition 3 of "Appendix" C shows that

$$h_{1\sigma,\sigma_2}(\theta) = h_{1\tau,\tau_2}(\theta + \omega(\sigma - \tau) + \omega(\tau_2 - \sigma_2)),$$
$$h_{2\sigma_2}(\theta) = h_{2\tau_2}(\theta + \omega(\sigma_2 - \tau_2)).$$

Similar to before, we will look for fixed points of $G^{(n)}$, that is, solutions to $\theta^* = G^{(n)}(\theta^*)$. If

$$\left| \frac{d}{d\theta} \right|_{\theta=\theta^*} (G^{(n)}(\theta)) \Big| < 1, \tag{27}$$

then the fixed point of $G^{(n)}$ is stable. Note that the relationship between fixed points of $G^{(n)}$ and clusters is more subtle for pulses with alternating properties than the relationship between fixed points of $g^{(n)}$ and n-clusters for identical pulses, because each τ-interval for the alternating case contains two pulses. This will be illustrated in the following examples.
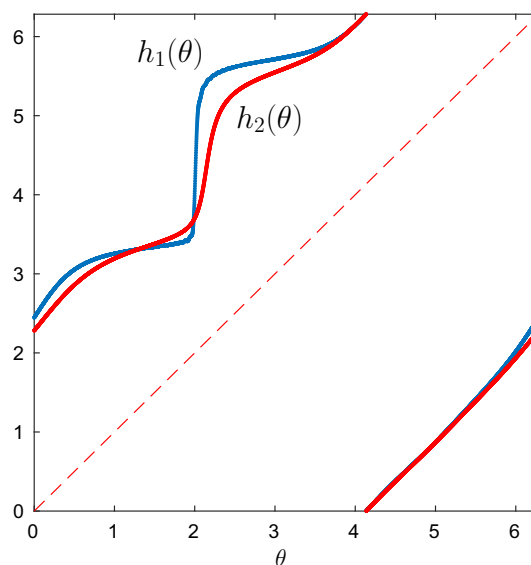

Fig. 15 Functions $h_1(\theta)$ for u_{max} corresponding to a current density of $20\mu A/cm^2$ and (red) $h_2(\theta)$ for u_{2max} corresponding to a current density of $10\mu A/cm^2$, for $\tau = 10$ ms and $\tau_2 = \tau/2$

Figure 15 shows $h_1(\theta)$ for u_{max} corresponding to a current density of $20\mu A/cm^2$ and $h_2(\theta)$ for u_{2max} corresponding to a current density of $10\mu A/cm^2$, for $\tau = 10$ ms and $\tau_2 = \tau/2$. We notice that these functions are quite similar to each other. Next, we show $G(\theta) = h_1(h_2(\theta))$ and $G^{(3)}(\theta)$ in Fig. 16, the latter for several different stimulation frequencies $1/\tau$. We see that for $\tau = 10$ ms (frequency 100 Hz) there is a stable period-3 orbit for G, corresponding to three stable fixed points for $G^{(3)}$. This corresponds to a 3-cluster state, as expected from Fig. 13 evaluated at 100 Hz. Here, the stable fixed points of $G^{(3)}$ correspond to a stable period-3 orbit of G, which in turn corresponds to a 3-cluster state. The lower panel shows that as the stimulation frequency increases, the $G^{(3)}$ function shifts right with small corrections according to (26), giving a saddlenode bifurcation in which the 3-cluster state disappears. We note that Fig. 16 for frequency 100 Hz looks very similar to Fig. 9 for identical pulses with frequency 100 Hz; however, the sequence of pulses is different. For Fig. 16, there is a "large" pulse at $t = 0$, a "small" pulse at $t = 5$ ms, another large pulse at $t = 10$ ms, another small pulse at $t = 15$ ms, another large pulse at $t = 20$ ms, etc. For Fig. 9 for 100 Hz, there is a large pulse at $t = 0$, another large pulse at $t = 10$ ms, another large pulse at $t = 20$ ms, etc, with no small pulses.

Figure 17 shows $G(\theta)$ and $G^{(2)}(\theta)$ for u_{max} corresponding to a current density of $20\mu A/cm^2$ and $h_2(\theta)$ for u_{2max} corresponding to a current density of $10\mu A/cm^2$, for $\tau = 6.67$ ms and $\tau_2 = \tau/2$. We see that there are four stable fixed points for $G^{(2)}$; these actually correspond to a 4-cluster state, as shown in Fig. 13 evaluated at 150 Hz. While at first it might seem surprising that stable fixed points for $G^{(2)}$ correspond
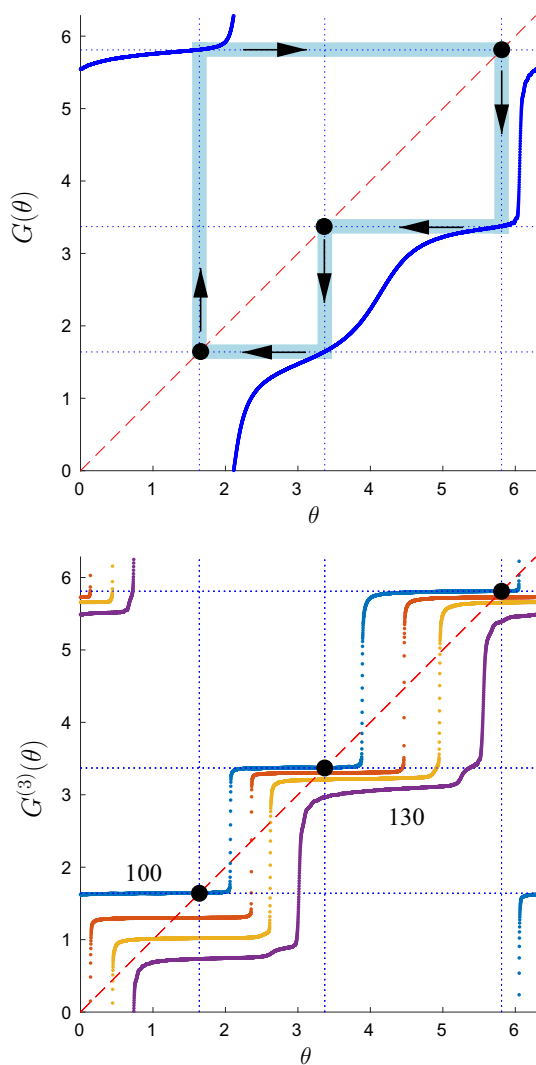
Fig. 16 Functions $G(\theta)$ and $G^{(3)}(\theta)$ for pulses with alternating properties with u_{max} corresponding to a current density of $20\mu A/cm^2$ and u_{2max} corresponding to a current density of $10\mu A/cm^2$. In the top panel, the stimulation frequency is 100 Hz ($\tau = 10$ ms), and $\tau_2 = \tau/2$. The bottom panel shows $G^{(3)}$ for stimulation frequencies of 100, 110, 120, and 130 Hz, all with $\tau_2 = \tau/2$

Fig. 17 Functions $G(\theta)$ and $G^{(2)}(\theta)$ for pulses with alternating properties with u_{max} corresponding to a current density of $20\mu A/cm^2$ and u_{2max} corresponding to a current density of $10\mu A/cm^2$, and $\tau = 6.67$ ms (corresponding to a stimulation frequency of 150 Hz), $\tau_2 = \tau/2$

to a 4-cluster state, we note that these results are similar to what we found for identical stimuli for a 300 Hz stimulus (or, equivalently, for alternating pulses with $\tau = 6.67$ ms and $u_{max} = u_{2max}$ corresponding to a current density of $20\mu A/cm^2$, $\tau_2 = \tau/2$). The proper comparison is that G for alternating pulses with a stimulation frequency of 150 Hz is similar to $g^{(2)}$ for identical pulses with a stimulation frequency of 300 Hz, and $G^{(2)}$ for alternating pulses for a stimulation frequency of 150 Hz is similar to $g^{(4)}$ for identical pulses with a stimulation frequency of 300 Hz. These results show that we can obtain 4-cluster solutions for a population of oscillators with these alternating pulses; see Fig. 18a.
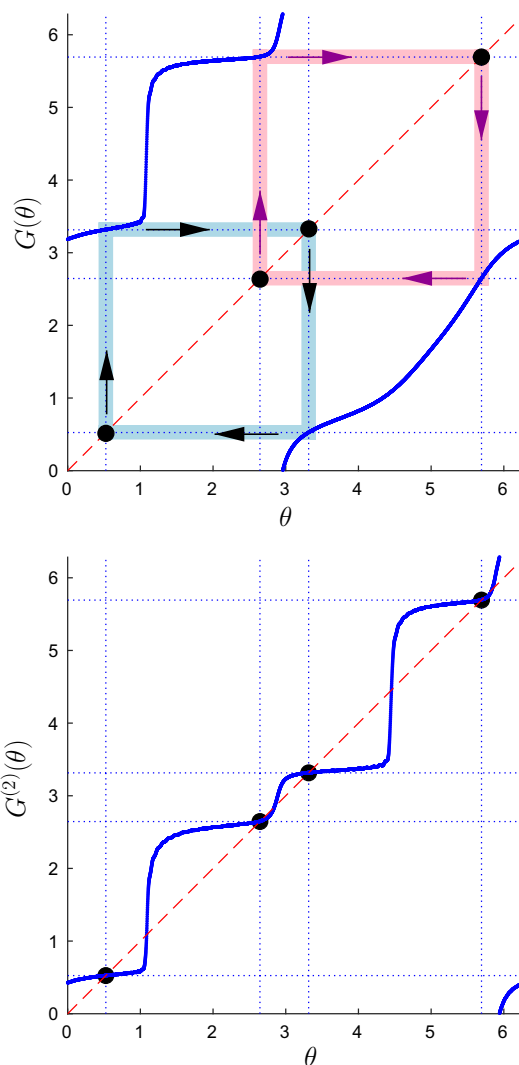
Our formulation also allows one to consider alternating pulses for which $\tau_2 \neq \tau/2$. For example, Fig. 19 shows results for u_{max} corresponding to $20\mu A/cm^2$, u_{2max} corresponding to $10\mu A/cm^2$, and $\tau_2 = 0.4\tau$ and $\tau_2 = 0.6\tau$. Interestingly, for $\tau_2 = 0.4\tau$ there are four fixed points of the $G^{(2)}$ map, corresponding to a 4-cluster solution, but for $\tau_2 = 0.6\tau$ there are only two fixed points of the $G^{(2)}$ map, corresponding to a 2-cluster solution. Figure 18b and c shows the corresponding time series for these cases. Comparing Figure 19 with the bottom panel of Figure 17, we deduce that if τ_2 is treated as a bifurcation parameter, there is a saddlenode bifurcation for τ_2 slightly larger than 0.5. This is as expected from (26), which implies that for new stimulation parameters σ and σ_2 satisfying $\sigma = \tau = 6.67$ and

(a) $\tau_2 = 0.5\tau$: 4 clusters

(b) $\tau_2 = 0.4\tau$: 4 clusters

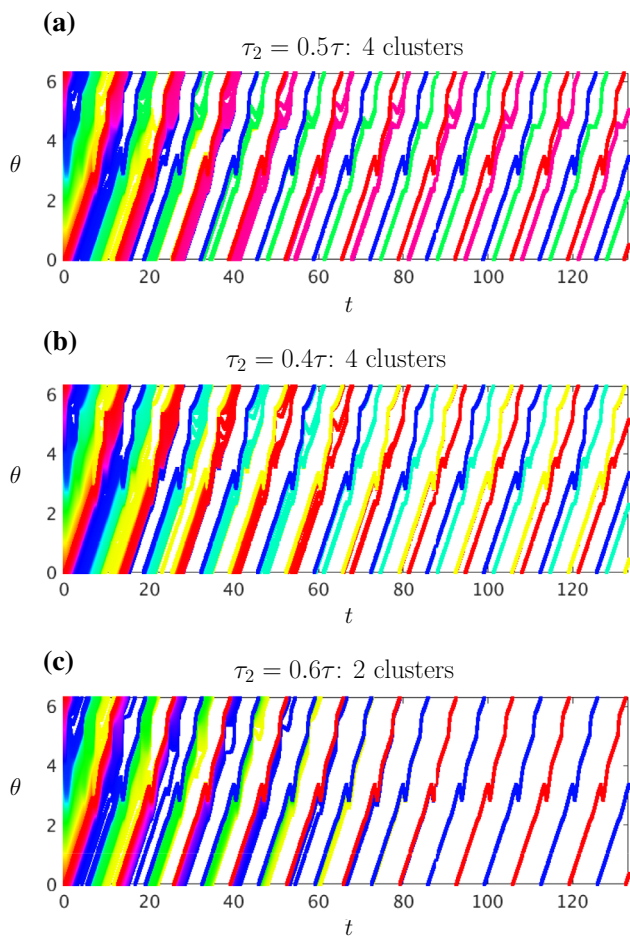**(c)** $\tau_2 = 0.6\tau$: 2 clusters

Fig. 18 Time series showing the phases of Hodgkin–Huxley neurons drawn from an initial uniform distribution with alternating pulses with u_{max} corresponding to $20\mu A/cm^2$ and u_{2max} corresponding to $10\mu A/cm^2$, for $\tau = 6.67$ ms and **a** $\tau_2 = 0.5\tau$, **b** $\tau_2 = 0.4\tau$, **c** $\tau_2 = 0.6\tau$. Four clusters form for (a) and (b), while only two clusters form for (c)

$0.6\tau = \sigma_2 > \tau_2 = 0.5\tau$, the $G^{(2)}$ map will shift left. Here, the shift is enough that a saddlenode bifurcation has occurred.

6 Conclusion

Populations of neural oscillators subjected to periodic pulsatile stimuli can display interesting clustering behavior, in which subpopulations of the neurons are synchronized, but the subpopulations are desynchronized with respect to each other. The details of the clustering behavior depend on the frequency and amplitude of the stimuli in a complicated way. Such clustering may be an important mechanism by which deep brain stimulation can lead to the alleviation of symptoms of Parkinson's disease and other disorders.

In this paper, we illustrated how the details of clustering for phase models of neurons subjected to periodic pulsatile inputs can be understood in terms of one-dimensional maps
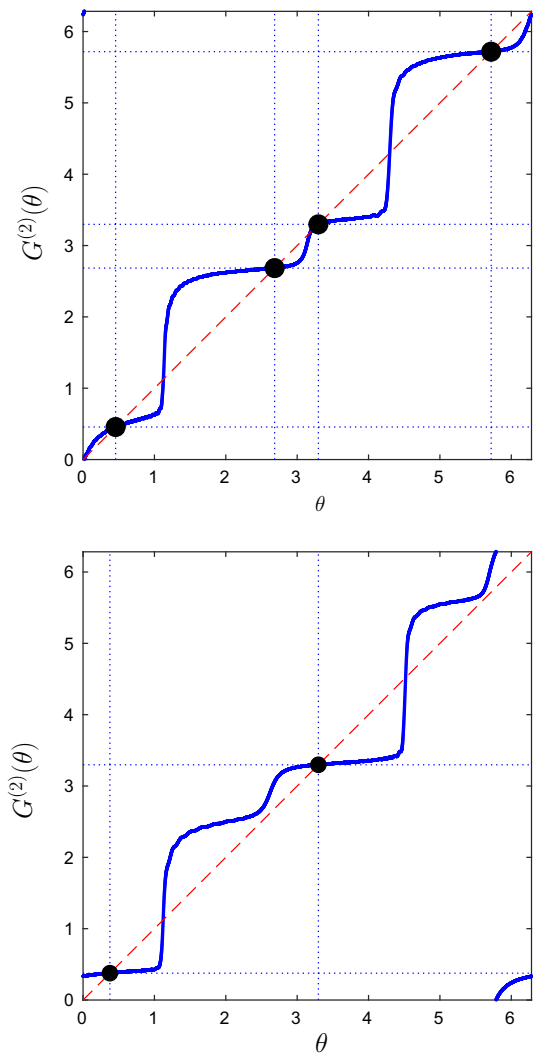

Fig. 19 Function $G^{(2)}(\theta)$ for alternating pulses with u_{max} corresponding to $20\mu A/cm^2$ and u_{2max} corresponding to $10\mu A/cm^2$, with $\tau = 6.67$ ms, and (top) $\tau_2 = 0.4\tau$ and (bottom) $\tau_2 = 0.6\tau$

defined on the circle. In particular, the analysis allows one to predict the number of clusters, their stability properties, their bifurcations, and their basins of attraction. Moreover, we generalized our analysis to consider stimuli with alternating properties, which provide additional degrees of freedom in the design of DBS stimuli.

As part of our study, we found multiple ways to get the same type of clustering behavior, for example by using identical pulses or pulses with alternating properties, or from stimuli with different parameters such as stimulation frequency or the time spacing between pulses with alternating properties. Such clustering occurs through the use of a single stimulation electrode, unlike coordinated reset which requires multiple electrodes. We expect that the same clustering behavior can also be obtained for different amplitudes of the pulses, cf. (Wilson and Moehlis 2015). We believe that the

analysis techniques used in this paper can be useful for identifying a collection of stimuli which give the same desirable clustering dynamics for a population of neurons, which will make it easier to find stimuli which are effective while minimizing the severity of side effects for DBS treatments. We note that this framework can also be used with other types of periodic stimuli besides (7) and also to help identify stimuli which lead to desynchronization while avoiding clustering, if that is a preferable control objective.

Our analysis assumed certain properties of a neural population: all neurons are identical, they all receive the same input, they are uncoupled, and there is no noise. For real neural populations, none of these assumptions would be valid. We also assumed that the phase models accurately capture the dynamics of the neurons, which is only true for sufficiently small inputs; see, for example, (Wilson and Ermentrout 2018). However, we believe that the results presented here form an important baseline for the analysis of more realistic neural populations stimulated by periodic pulses. We note that the effect of noise on periodically forced neural populations has been considered in Wilson and Moehlis (2015), which shows that for weak noise and long times, the number of neurons in each cluster is roughly the same. We expect that similar results will hold for neurons in the presence of weak noise subjected to alternating stimuli.

Our hope is that the techniques in this paper will help to guide the design of stimuli for the treatment of Parkinson's disease and other disorders. We believe that the use of pulses with alternating properties is particularly worthy of further investigation, since it represents a larger class of stimuli than has been considered in previous studies.

Appendix A: neuron models

In this appendix, we give details of the neural models used in this paper, specifically the Hodgkin–Huxley model considered in the main text, and the thalamic neuron model considered in Appendix B.

Hodgkin–Huxley neuron model

The full Hodgkin–Huxley model is given by:

$$\dot{V} = (I_b - \bar{g}_{Na}h(V - V_{Na})m^3 - \bar{g}_K(V - V_K)n^4$$
$$- \bar{g}_L(V - V_L))/c + u(t) ,$$
$$\dot{m} = a_m(V)(1 - m) - b_m(V)m ,$$
$$\dot{h} = a_h(V)(1 - h) - b_h(V)h ,$$
$$\dot{n} = a_n(V)(1 - n) - b_n(V)n ,$$

where

$$a_m(V) = 0.1(V + 40)/(1 - \exp(-(V + 40)/10)) ,$$
$$b_m(V) = 4\exp(-(V + 65)/18) ,$$
$$a_h(V) = 0.07\exp(-(V + 65)/20) ,$$
$$b_h(V) = 1/(1 + \exp(-(V + 35)/10)) ,$$
$$a_n(V) = 0.01(V + 55)/(1 - \exp(-(V + 55)/10)) ,$$
$$b_n(V) = 0.125\exp(-(V + 65)/80) ,$$

The parameters for this model are

$$V_{Na} = 50 \, mV , \quad V_K = -77 \, mV , \quad V_L = -54.4 \, mV ,$$
$$\bar{g}_{Na} = 120 \, mS/cm^2 , \quad \bar{g}_K = 36 \, mS/cm^2 ,$$
$$\bar{g}_L = 0.3 \, mS/cm^2 , \quad I_b = 10 \, \mu A/cm^2 ,$$
$$c = 1 \, \mu F/cm^2 .$$

Thalamic neuron model

The full thalamic neuron model is given by:

$$\dot{V} = \frac{-I_L - I_{Na} - I_K - I_T + I_b}{C_m} + u(t),$$
$$\dot{h} = \frac{h_\infty - h}{\tau_h},$$
$$\dot{r} = \frac{r_\infty - r}{\tau_r},$$

where

$$h_\infty = 1/(1 + \exp((V + 41)/4)),$$
$$r_\infty = 1/(1 + \exp((V + 84)/4)),$$
$$\alpha_h = 0.128\exp(-(V + 46)/18),$$
$$\beta_h = 4/(1 + \exp(-(V + 23)/5)),$$
$$\tau_h = 1/(\alpha_h + \beta_h),$$
$$\tau_r = (28 + \exp(-(V + 25)/10.5)),$$
$$m_\infty = 1/(1 + \exp(-(V + 37)/7)),$$
$$p_\infty = 1/(1 + \exp(-(V + 60)/6.2)),$$
$$I_L = g_L(V - e_L),$$
$$I_{Na} = g_{Na}(m_\infty^3)h(V - e_{Na}),$$
$$I_K = g_K((0.75(1 - h))^4)(V - e_K),$$
$$I_T = g_T(p_\infty^2)r(V - e_T).$$

The parameters for this model are

$$C_m = 1 \, \mu F/cm^2 , \quad g_L = 0.05 \, mS/cm^2 , \quad e_L = -70 \, mV ,$$
$$g_{Na} = 3 \, mS/cm^2 , \quad e_{Na} = 50 \, mV, \quad g_K = 5 \, mS/cm^2 ,$$
$$e_K = -90 \, mV , \quad g_T = 5 \, mS/cm^2 , \quad e_T = 0 \, mV ,$$
$$I_b = 5 \, \mu A/cm^2 .$$

Appendix B: results for thalamic neurons

In this appendix, we show simulations and analysis for an (approximately) Type I neuron model, the thalamic neurons from (Rubin and Terman 2004). The full equations are given in Appendix A; for our simulations, we use the corresponding phase model. For reference, for these parameters the thalamic neurons have $\omega = 0.748$ rad/s.

We consider populations of thalamic neurons with the same stimuli (7) with u_{max} corresponding to a current density of 20 $\mu A/cm^2$, $p = 0.5$ ms, and $\lambda = 3$. We simulated 500 thalamic neurons with initial phases evenly spaced between 0 and 2π, corresponding to a uniform distribution. The stimulation frequency was varied from 70 Hz to 300 Hz in increments of 5 Hz. Figure 20 shows the final phases after 40 periods of stimulation, after transients have decayed. Figure 21 shows the time series of the phases of a population of such neurons for selected frequencies. Here, we again see clustering for some frequencies (such as 250 Hz, where r_2 is large and r_1 and r_3 are small, indicating a 2-cluster solution), and non-clustering behavior for other frequencies (such as 200 Hz, where the Lyapunov exponent Λ is positive, corresponding to chaotic dynamics).

The same analysis techniques can also be used to understand the dynamics of thalamic neurons subjected to periodic pulses. Figure 22a shows the response function $f(\theta)$ for thalamic neurons with the stimulus given by (7) with u_{max} corresponding to a current density of $20\mu A/cm^2$, $p = 0.5$ ms, and $\lambda = 3$; Fig. 22b shows that there is a stable 2-cluster state for a stimulation frequency of 250 Hz, as expected from Fig. 20.

Fig. 20 **a** The final phases θ of thalamic neurons drawn from an initial uniform distribution as a function of stimulation frequency, after 40 periods of stimulation. Colors correspond to the neurons' initial phases. **b** Order parameters r_1 (black), r_2 (blue), and r_3 (red) for the final state as a function of frequency. For the initial uniform distribution, $r_1 = r_2 = r_3 = 0$. **c** Lyapunov exponent Λ as a function of stimulation frequency

Appendix C: shift properties of the maps

Proposition 1 *(**Shift properties of** $g^{(n)}$): Iterates of the map*

$$g_\tau(\theta) = \theta + \omega\tau + f(\theta + \omega\tau) \tag{28}$$

satisfy the property

$$g_\sigma^{(n)}(\theta) = g_\tau^{(n)}(\theta + \omega(\sigma - \tau)) + \mathcal{O}(\sigma - \tau). \tag{29}$$

Proof We will prove this by induction. First, (29) holds for $n = 1$ from (19) in the main text (in fact, in this case the $\mathcal{O}(\sigma - \tau)$ correction term vanishes). Next, let us assume that (29) holds for n; we will show that this implies that it also holds for $n + 1$. For reference,

$$\begin{aligned} g_\tau^{(n+1)}(\theta) &= g_\tau(g_\tau^{(n)}(\theta)) \\ &= g_\tau^{(n)}(\theta) + \omega\tau + f(g_\tau^{(n)}(\theta) + \omega\tau). \end{aligned} \tag{30}$$
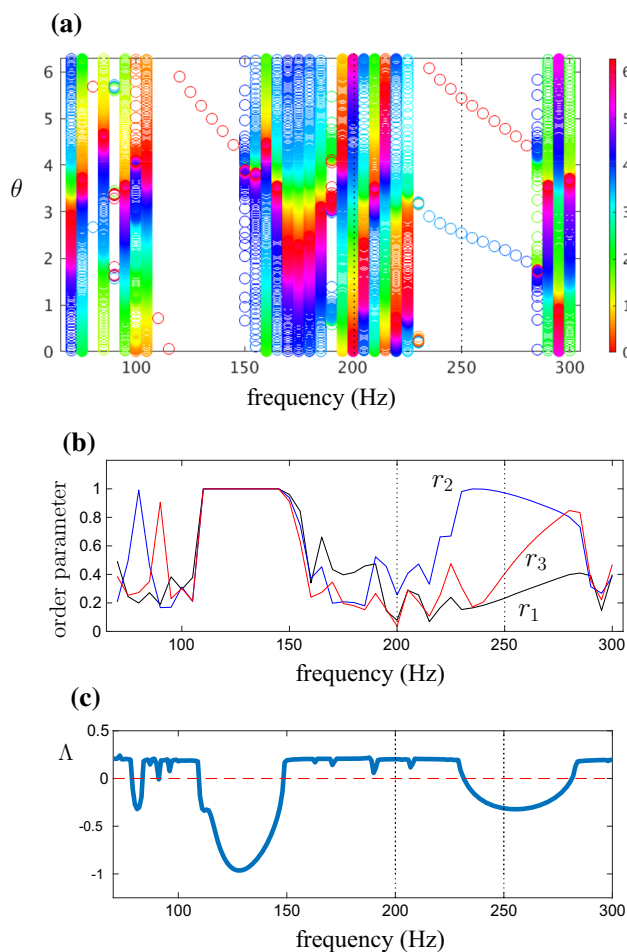
Now,

$$\begin{aligned} g_\sigma^{(n+1)}(\theta) &= g_\sigma(g_\sigma^{(n)}(\theta)) \\ &= g_\sigma^{(n)}(\theta) + \omega\sigma + f(g_\sigma^{(n)}(\theta) + \omega\sigma) \\ &= g_\tau^{(n)}(\theta + \omega(\sigma - \tau)) + \mathcal{O}(\sigma - \tau) + \omega\sigma \\ &\quad + f(g_\tau^{(n)}(\theta + \omega(\sigma - \tau)) + \mathcal{O}(\sigma - \tau) + \omega\sigma), \end{aligned}$$

where we have used (29). We now use $\omega\sigma = \omega\tau + \omega(\sigma - \tau) = \omega\tau + \mathcal{O}(\sigma - \tau)$ to give

$$\begin{aligned} g_\sigma^{(n+1)}(\theta) &= g_\tau^{(n)}(\theta + \omega(\sigma - \tau)) + \omega\tau + \mathcal{O}(\sigma - \tau) \\ &\quad + f(g_\tau^{(n)}(\theta + \omega(\sigma - \tau)) + \omega\tau + \mathcal{O}(\sigma - \tau)). \end{aligned}$$
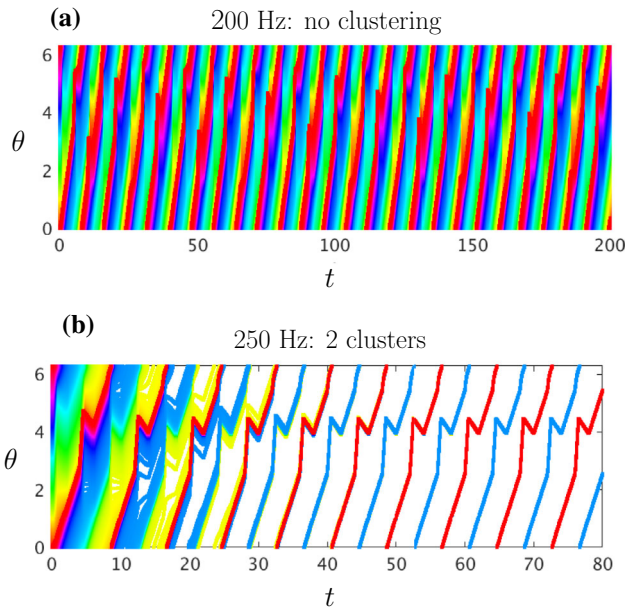
(a) 200 Hz: no clustering

(b) 250 Hz: 2 clusters

Fig. 21 Time series showing the phases of thalamic neurons drawn from an initial uniform distribution for frequencies **a** 200 Hz, and **b** 250 Hz. For (a), clusters do not form; for (b), there are two clusters after transients decay away

Next, we Taylor expand the last term about $g_\tau^{(n)}(\theta + \omega(\sigma - \tau)) + \omega\tau$, treating $(\sigma - \tau)$ as small:

$$f(g_\tau^{(n)}(\theta + \omega(\sigma - \tau)) + \omega\tau + \mathcal{O}(\sigma - \tau))$$
$$= f(g_\tau^{(n)}(\theta + \omega(\sigma - \tau)) + \omega\tau) + \mathcal{O}(\sigma - \tau)$$

Thus,

$$g_\sigma^{(n+1)}(\theta) = g_\tau^{(n)}(\theta + \omega(\sigma - \tau)) + \omega\tau$$
$$+ f(g_\tau^{(n)}(\theta + \omega(\sigma - \tau)) + \omega\tau) + \mathcal{O}(\sigma - \tau)$$
$$= g_\tau^{(n+1)}(\theta + \omega(\sigma - \tau)) + \mathcal{O}(\sigma - \tau),$$

where the last equality follows from (30). Therefore, (29) holds for all $n \geq 1$, with no $\mathcal{O}(\sigma - \tau)$ term necessary for $n = 1$ from (19).

Proposition 2 *(**Shift properties of** $G^{(n)}$): Iterates of the map*

$$G_{\tau,\tau_2}(\theta) = \theta + \omega\tau + f_2(\theta + \omega\tau_2)$$
$$+ f(\theta + \omega\tau + f_2(\theta + \omega\tau_2)) \quad (31)$$

satisfy the property

$$G_{\sigma,\sigma_2}^{(n)} = G_{\tau,\tau_2}^{(n)}(\theta + \omega(\sigma - \tau) + \omega(\sigma_2 - \tau_2))$$
$$+ \mathcal{O}(\sigma - \tau) + \mathcal{O}(\sigma_2 - \tau_2). \quad (32)$$
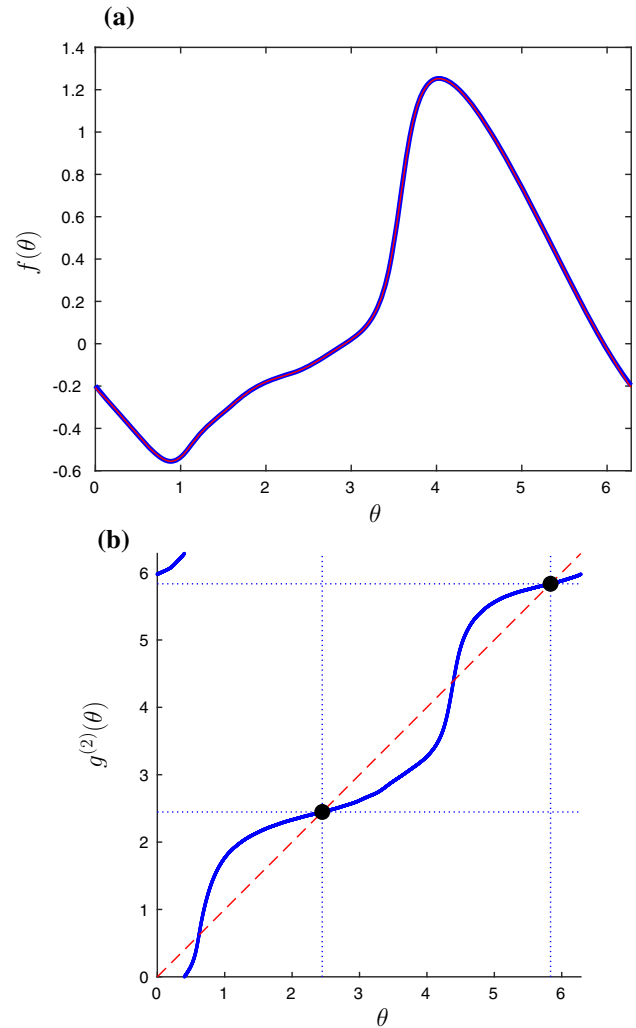

Fig. 22 **a** Response function $f(\theta)$ which characterizes the phase response of thalamic neurons to a pulse with u_{max} corresponding to a current of $20\mu A/cm^2$, $p = 0.5$ ms, and $\lambda = 3$. **b** Map $g^{(2)}(\theta)$ for the thalamic neuron with stimulation frequency 250 Hz, showing two stable fixed points which correspond to a 2-cluster state

Proof We will prove this using induction. Let us first show that (32) holds for $n = 1$. By definition,

$$G_{\sigma,\sigma_2}(\theta) = \theta + \omega\sigma + f_2(\theta + \omega\sigma_2)$$
$$+ f(\theta + \omega\sigma + f_2(\theta + \omega\sigma_2)).$$

Letting

$$\theta = \hat{\theta} + \omega(\tau - \sigma) + \omega(\tau_2 - \sigma_2),$$

and simplifying, we obtain

$$G_{\sigma,\sigma_2}(\theta) = \hat{\theta} + \omega\tau - \omega(\sigma_2 - \tau_2)$$
$$+ f_2(\hat{\theta} + \omega\tau_2 - \omega(\sigma - \tau))$$
$$+ f(\hat{\theta} + \omega\tau - \omega(\sigma_2 - \tau_2))$$

$$+f_2(\hat{\theta} + \omega\tau_2 - \omega(\sigma - \tau)))$$
$$= \hat{\theta} + \omega\tau + f_2(\hat{\theta} + \omega\tau_2)$$
$$\quad + f(\hat{\theta} + \omega\tau + f_2(\hat{\theta} + \omega\tau_2))$$
$$\quad + \mathcal{O}(\sigma - \tau) + \mathcal{O}(\sigma_2 - \tau_2)$$
$$= G_{\tau,\tau_2}(\hat{\theta}) + \mathcal{O}(\sigma - \tau) + \mathcal{O}(\sigma_2 - \tau_2)$$
$$= G_{\tau,\tau_2}(\theta + \omega(\sigma - \tau) + \omega(\sigma_2 - \tau_2))$$
$$\quad + \mathcal{O}(\sigma - \tau) + \mathcal{O}(\sigma_2 - \tau_2).$$

Here, the second equality follows from Taylor expansion, treating $(\sigma - \tau)$ and $(\sigma_2 - \tau_2)$ as small. Thus, (32) holds for $n = 1$.

Now, suppose (32) holds for n; we will show this also implies that it holds for $n + 1$. For reference,

$$G_{\tau,\tau_2}^{(n+1)}(\theta) = G_{\tau,\tau_2}(G_{\tau,\tau_2}^{(n)}(\theta))$$
$$= G_{\tau,\tau_2}^{(n)}(\theta) + \omega\tau + f_2(G_{\tau,\tau_2}^{(n)}(\theta) + \omega\tau_2)$$
$$\quad + f(G_{\tau,\tau_2}^{(n)}(\theta) + \omega\tau + f_2(G_{\tau,\tau_2}^{(n)}(\theta) + \omega\tau_2)).$$
$$\tag{33}$$

Now,

$$G_{\sigma,\sigma_2}^{(n+1)}(\theta) = G_{\sigma,\sigma_2}(G_{\sigma,\sigma_2}^{(n)}(\theta))$$
$$= G_{\sigma,\sigma_2}^{(n)}(\theta) + \omega\sigma + f_2(G_{\sigma,\sigma_2}^{(n)}(\theta) + \omega\sigma_2)$$
$$\quad + f(G_{\sigma,\sigma_2}^{(n)}(\theta) + \omega\sigma + f_2(G_{\sigma,\sigma_2}^{(n)}(\theta) + \omega\sigma_2))$$
$$= G_{\tau,\tau_2}^{(n)}(\theta + \omega(\sigma - \tau) + \omega(\sigma_2 - \tau_2))$$
$$\quad + \mathcal{O}(\sigma - \tau) + \mathcal{O}(\sigma_2 - \tau_2) + \omega\sigma$$
$$\quad + f_2(G_{\tau,\tau_2}^{(n)}(\theta + \omega(\sigma - \tau) + \omega(\sigma_2 - \tau_2))$$
$$\quad\quad + \mathcal{O}(\sigma - \tau) + \mathcal{O}(\sigma_2 - \tau_2) + \omega\sigma_2)$$
$$\quad + f(G_{\tau,\tau_2}^{(n)}(\theta + \omega(\sigma - \tau) + \omega(\sigma_2 - \tau_2))$$
$$\quad\quad + \mathcal{O}(\sigma - \tau) + \mathcal{O}(\sigma_2 - \tau_2) + \omega\sigma$$
$$\quad\quad + f_2(G_{\tau,\tau_2}^{(n)}(\theta + \omega(\sigma - \tau) + \omega(\sigma_2 - \tau_2))$$
$$\quad\quad + \mathcal{O}(\sigma - \tau) + \mathcal{O}(\sigma_2 - \tau_2) + \omega\sigma_2)),$$

where the last equality follows from (32). Letting

$$\omega\sigma = \omega\tau + \omega(\sigma - \tau) = \omega\tau + \mathcal{O}(\sigma - \tau)$$

and

$$\omega\sigma_2 = \omega\tau_2 + \omega(\sigma_2 - \tau_2) = \omega\tau_2 + \mathcal{O}(\sigma_2 - \tau_2),$$
$$G_{\sigma,\sigma_2}^{(n+1)}(\theta) = G_{\tau,\tau_2}^{(n)}(\theta + \omega(\sigma - \tau) + \omega(\sigma_2 - \tau_2))$$
$$\quad + \omega\tau + \mathcal{O}(\sigma - \tau) + \mathcal{O}(\sigma_2 - \tau_2)$$
$$\quad + f_2(G_{\tau,\tau_2}^{(n)}(\theta + \omega(\sigma - \tau) + \omega(\sigma_2 - \tau_2))$$
$$\quad\quad + \omega\tau_2 + \mathcal{O}(\sigma - \tau) + \mathcal{O}(\sigma_2 - \tau_2))$$
$$\quad + f(G_{\tau,\tau_2}^{(n)}(\theta + \omega(\sigma - \tau) + \omega(\sigma_2 - \tau_2))$$
$$\quad\quad + \omega\tau + \mathcal{O}(\sigma - \tau) + \mathcal{O}(\sigma_2 - \tau_2)$$

$$\quad\quad + f_2(G_{\tau,\tau_2}^{(n)}(\theta + \omega(\sigma - \tau) + \omega(\sigma_2 - \tau_2))$$
$$\quad\quad + \omega\tau_2 + \mathcal{O}(\sigma - \tau) + \mathcal{O}(\sigma_2 - \tau_2))).$$

Finally, treating $(\sigma - \tau)$ and $(\sigma_2 - \tau_2)$ as small and Taylor expanding f and f_2,

$$G_{\sigma,\sigma_2}^{(n+1)}(\theta) = G_{\tau,\tau_2}^{(n)}(\theta + \omega(\sigma - \tau) + \omega(\sigma_2 - \tau_2)) + \omega\tau$$
$$\quad + f_2(G_{\tau,\tau_2}^{(n)}(\theta + \omega(\sigma - \tau)$$
$$\quad\quad + \omega(\sigma_2 - \tau_2)) + \omega\tau_2)$$
$$\quad + f(G_{\tau,\tau_2}^{(n)}(\theta + \omega(\sigma - \tau) + \omega(\sigma_2 - \tau_2)) + \omega\tau$$
$$\quad\quad + f_2(G_{\tau,\tau_2}^{(n)}(\theta + \omega(\sigma - \tau)$$
$$\quad\quad + \omega(\sigma_2 - \tau_2)) + \omega\tau_2))$$
$$\quad + \mathcal{O}(\sigma - \tau) + \mathcal{O}(\sigma_2 - \tau_2)$$
$$= G_{\tau,\tau_2}^{(n+1)}(\theta + \omega(\sigma - \tau) + \omega(\sigma_2 - \tau_2))$$
$$\quad + \mathcal{O}(\sigma - \tau) + \mathcal{O}(\sigma_2 - \tau_2),$$

as desired, where the last equality follows from (33). Thus, (32) holds for all $n \geq 1$.

Proposition 3 *(**Shift properties of h_1 and h_2**): The maps*

$$h_{1\tau,\tau_2}(\theta) = \theta + \omega(\tau - \tau_2) + f(\theta + \omega(\tau - \tau_2)) \tag{34}$$
$$h_{2\tau_2}(\theta) = \theta + \omega\tau_2 + f_2(\theta + \omega\tau_2) \tag{35}$$

satisfy the properties

$$h_{1\sigma,\sigma_2}(\theta) = h_{1\tau,\tau_2}(\theta + \omega(\sigma - \tau) + \omega(\tau_2 - \sigma_2)), \tag{36}$$
$$h_{2\sigma_2}(\theta) = h_{2\tau_2}(\theta + \omega(\sigma_2 - \tau_2)). \tag{37}$$

Proof First, consider

$$h_{1\sigma,\sigma_2}(\theta) = \theta + \omega(\sigma - \sigma_2) + f(\theta + \omega(\sigma - \sigma_2)).$$

Letting

$$\theta = \hat{\theta} + \omega(\tau - \sigma) + \omega(\sigma_2 - \tau_2)$$

and simplifying,

$$h_{1\sigma,\sigma_2}(\theta) = \hat{\theta} + \omega(\tau - \tau_2) + f(\hat{\theta} + \omega(\tau - \tau_2))$$
$$= h_{1\tau,\tau_2}(\hat{\theta})$$
$$= h_{1\tau,\tau_2}(\theta + \omega(\sigma - \tau) + \omega(\tau_2 - \sigma_2)).$$

Now, consider

$$h_{2\sigma_2}(\theta) = \theta + \omega\sigma_2 + f_2(\theta + \omega\sigma_2).$$

Letting

$$\theta = \hat{\theta} + \omega(\tau_2 - \sigma_2)$$

and simplifying,

$$h_{2\sigma_2}(\theta) = \hat{\theta} + \omega\tau_2 + f(\hat{\theta} + \omega\tau_2) = h_{2\tau_2}(\hat{\theta})$$
$$= h_{2\tau_2}(\theta + \omega(\sigma_2 - \tau_2)).$$

References

Adamchic I, Hauptmann C, Barnikol UB, Pawelczyk N, Popovych O, Barnikol TT, Silchenko A, Volkmann J, Deuschl G, Meissner WG, Maarouf M, Sturm V, Freund HJ, Tass PA (2014) Coordinated reset neuromodulation for Parkinson's disease: proof-of-concept study. Mov Disord 29(13):1679–1684

Benabid A, Benazzous A, Pollak P (2002) Mechanisms of deep brain stimulation. Movement Disorders 17(SUPPL. 3):19–38

Benabid AL, Pollak P, Gervason C, Hoffmann D, Gao DM, Hommel M, Perret JE, Rougemont JD (1991) Long-term suppression of tremor by chronic stimulation of the ventral intermediate thalamic nucleus. Lancet 337:403–406

Best D, Fisher N (1979) Efficient simulation of the von Mises distribution. J R Stat Soc Ser C Appl Stat 28:152–157

Brown E, Moehlis J, Holmes P (2004) On the phase reduction and response dynamics of neural oscillator populations. Neural Comp 16:673–715

Buhmann C, Huckhagel T, Engel K, Gulberti A, Hidding U, Poetter-Nerger M, Goerendt I, Ludewig P, Braass H, Choe C et al (2017) Adverse events in deep brain stimulation: a retrospective long-term analysis of neurological psychiatric and other occurrences. PLoS One 12:e0178984

Chen C, Litvak V, Gilbertson T, Kuhn A, Lu C, Lee S, Tsai C, Tisch S, Limousin P, Hariz M, Brown P (2007) Excessive synchronization of basal ganglia neurons at 20 hz slows movement in Parkinson's disease. Experim Neurol 205:214–221

Chiken S, Nambu A (2016) Mechanism of deep brain stimulation: inhibition, excitation, or disruption? Neuroscientist 22:313–322

Cyron D (2016) Mental side effects of deep brain stimulation (DBS) for movement disorders: the futility of denial. Front Integr Neurosci 10:17

Daido H (1996) Onset of cooperative entrainment in limit-cycle oscillators with uniform all-to-all interactions: bifurcation of the order function. Phys D 91:24–66

Ermentrout G (2002) Simulating, Analyzing, and Animating Dynamical Systems: A Guide to XPPAUT for Researchers and Students. SIAM, Philadelphia

Ermentrout G, Kopell N (1998) Fine structure of neural spiking and synchronization in the presence of conduction delays. Proc Natl Acad Sci USA 95:1259–1264

Ermentrout GB, Terman DH (2010) Mathematical Foundations of Neuroscience. Springer, Berlin

Glass L, Mackey MC (1988) From Clocks to Chaos: the Rhythms of Life. Princeton University Press, Princeton

Guckenheimer J (1975) Isochrons and phaseless sets. J Math Biol 1:259–273

Hammond C, Bergman H, Brown P (2007) Pathological synchronization in parkinson's disease: networks, models and treatments. Trends Neurosci 30:357–364

Herrington T, Cheng J, Eskandar E (2016) Mechanisms of deep brain stimulation. J Neurophysiol 115:19–38

Hodgkin AL, Huxley AF (1952) A quantitative description of membrane current and its application to conduction and excitation in nerve. J Physiol 117:500–544

Keener J, Hoppensteadt F, Rinzel J (1981) Integrate-and-fire models of nerve membrane response to oscillatory input. SIAM J ono Appl Math 41:503–517

Kuncel AM, Grill WM (2004) Selection of stimulus parameters for deep brain stimulation. Clin Neurophysiol 115(11):2431–2441

Kuramoto Y (1984) Chemical Oscillations, Waves, and Turbulence. Springer, Berlin

Levy R, Hutchison W, Lozano A, Dostrovsky J (2000) High-frequency synchronization of neuronal activity in the subthalamic nucleus of Parkinsonian patients with limb tremor. J Neurosci 20:7766–7775

Liu Y, Postupna N, Falkenberg J, Anderson M (2008) High frequency deep brain stimulation: what are the therapeutic mechanisms? Neurosci Biobehav Rev 32:343–351

Lücken L, Yanchuk S, Popovych O, Tass P (2013) Desynchronization boost by non-uniform coordinated reset stimulation in ensembles of pulse-coupled neurons. Front Comput Neurosci 7:63

Lysyansky B, Popovych O, Tass P (2011) Desynchronizing anti-resonance effect of m: n ON-OFF coordinated reset stimulation. J Neural Eng 8:036019

Lysyansky B, Popovych O, Tass P (2013) Optimal number of stimulation contacts for coordinated reset neuromodulation. Front Neuroeng 6:5

Matchen T, Moehlis J (2018) Phase model-based neuron stabilization into arbitrary clusters. Journal of Computational Neuroscience 44:363–378

Monga B, Moehlis J (2019) Phase distribution control of a population of oscillators. Phys D 398:115–129

Monga B, Moehlis J (2020) Supervised learning algorithms for control of underactuated dynamical systems. Phys D 412:132621

Monga B, Wilson D, Matchen T, Moehlis J (2019) Phase reduction and phase-based optimal control for biological systems: a tutorial. Biol Cybern 113:11–46

Montgomery E (2010) Deep Brain Stimulation Programming: principles and Practice. Oxford University Press, Oxford

Moro E, Esselink RJ, Xie J, Hommel M, Benabid AL, Pollak P (2002) The impact on Parkinson's disease of electrical parameter settings in STN stimulation. Neurology 59(5):706–713

Nabi A, Mirzadeh M, Gibou F, Moehlis J (2013) Minimum energy desynchronizing control for coupled neurons. J Comp Neuro 34:259–271

Netoff T, Schwemmer M, Lewis T (2012) Experimentally estimating phase response curves of neurons: theoretical and practical issues. In: Schultheiss N, Prinz A, Butera R (eds) Phase Response Curves in Neuroscience. Springer, Berlin, pp 95–129

Ott E (1993) Chaos in Dynamical Systems. Cambridge University Press, Cambridge

Rizzone M, Lanotte M, Bergamasco B, Tavella A, Torre E, Faccani G, Melcarne A, Lopiano L (2001) Deep brain stimulation of the subthalamic nucleus in Parkinson's disease: effects of variation in stimulation parameters. J Neurol Neurosurg Psychiatr 71(2):215–219

Rosenbaum R, Zimnik A, Zheng F, Turner R, Alzheimer C, Doiron B, Rubin J (2014) Axonal and syntaptic failure suppress the transfer of firing rate oscillations, synchrony and information during high frequency deep brain stimulation. Neurobiol Dis 62:86–99

Rubin J, Terman D (2004) High frequency stimulation of the subthalamic nucleus eliminates pathological thalamic rhythmicity in a computational model. J Comput Neurosci 16(3):211–235

Savica R, Stead M, Mack K, Lee K, Klassen B (2012) Deep brain stimulation in Tourette syndrome: a description of 3 patients with excellent outcome. Mayo Clinic Proc 87:59–62

Schnitzler A, Gross J (2005) Normal and pathological oscillatory communication in the brain. Nat Rev Neurosci 6:285–296

Tass PA (2003) A model of desynchronizing deep brain stimulation with a demand-controlled coordinated reset of neural subpopulations. Biol Cybern 89(2):81–88

Tass PA (2003) Desynchronization by means of a coordinated reset of neural sub-populations—A novel technique for demand-

controlled deep brain stimulation. Progress Theor Phys Suppl 150:281–296

Uhlhaas P, Singer W (2006) Neural synchrony in brain disorders: relevance for cognitive dysfunctions and pathophysiology. Neuron 52:155–168

Volkmann J, Herzog J, Kopper F, Deuschl G (2002) Introduction to the programming of deep brain stimulators. Mov Disord 17(Suppl 3):S181–187

Wilson CJ, Beverlin B, Netoff T (2011) Chaotic desynchronization as the therapeutic mechanism of deep brain stimulation. Front Syst Neurosci 5:50

Wilson D (2020) Optimal open-loop desynchronization of neural oscillator populations. J Math Biol 81:25–64

Wilson D, Ermentrout B (2018) Greater accuracy and broadened applicability of phase reduction using isostable coordinates. J Math Biol 76(1–2):37–66

Wilson D, Moehlis J (2014) Optimal chaotic desynchronization for neural populations. SIAM J Appl Dyn Syst 13:276–305

Wilson D, Moehlis J (2015) Clustered desynchronization from high-frequency deep brain stimulation. PLoS Comput Biol 11(12):e1004673

Winfree A (1967) Biological rhythms and the behavior of populations of coupled oscillators. J Theor Biol 16:14–42

Winfree A (2001) The Geometry of Biological Time, 2nd edn. Springer, New York